

IXPE Science Operations Center		
Title: User Guide — Observatory	Document No.: IXPE-SOC-DOC-011	Revision: A
	Effective Date: 2022-07-22	Page: 1 of 69



National Aeronautics and  
Space Administration

**IXPE-SOC-DOC-011**

Revision A

EFFECTIVE DATE: 2022-07-22

**George C. Marshall Space Flight Center**  
Marshall Space Flight Center, Alabama 35812

ST-12

IMAGING X-RAY POLARIMETRY EXPLORER  
(IXPE)  
SCIENCE OPERATIONS CENTER (SOC)

User Guide — Observatory

IXPE Science Operations Center  
User Guide to the Observatory

IXPE Science Operations Center		
Title: User Guide — Observatory	Document No.: IXPE-SOC-DOC-011	Revision: A
	Effective Date: 2022-07-22	Page: 2 of 69

## Signatures

APPROVED BY

---

Kurt Dietz/ ES63  
SOC Software Lead

---

Allyn F. Tennant /ST12  
SOC Lead

---

Stephen L. O'Dell /ST12  
Project Scientist

---

Brian D. Ramsey /ST12  
Deputy Principal Investigator

<b>IXPE Science Operations Center</b>		
<b>Title: User Guide — Observatory</b>	<b>Document No.: IXPE-SOC-DOC-011</b>	<b>Revision: A</b>
	<b>Effective Date: 2022-07-22</b>	<b>Page: 3 of 69</b>

## Revision Log

Date	Rev	Notes
2022-03-22	Baseline	Baseline version
2022-07-15	A	Formatting changes to improve consistency with other IXPE User Guides

<b>IXPE Science Operations Center</b>		
<b>Title: User Guide — Observatory</b>	<b>Document No.: IXPE-SOC-DOC-011</b>	<b>Revision: A</b>
	<b>Effective Date: 2022-07-22</b>	<b>Page: 4 of 69</b>

## TABLE OF CONTENTS

1.	MISSION OVERVIEW .....	7
2.	GROUND SYSTEM.....	8
	2.1. OVERVIEW .....	8
	2.2. DOWNLINK AND UPLINK CAPABILITY .....	9
	2.3. MISSION OPERATIONS CENTER (MOC).....	9
	2.4. SCIENCE OPERATIONS CENTER (SOC).....	9
	2.4.1. DATA PRODUCTS .....	10
	2.4.2. OBSERVATION SCHEDULE.....	10
	2.4.2.1. TARGET VISIBILITY .....	10
	2.4.2.2. TARGETS OF OPPORTUNITY .....	10
3.	ATTITUDE DETERMINATION AND CONTROL .....	10
	3.1. SYSTEM.....	10
	3.1.1. GPS RECEIVER .....	11
	3.1.2. STAR TRACKER .....	11
	3.2. SLEW CAPABILITY .....	11
4.	PAYLOAD .....	11
	4.1. TELESCOPES .....	11
	4.2. IXPE COILABLE BOOM.....	12
	4.3. X-RAY SHIELDS .....	12
	4.4. TELESCOPE ALIGNMENT.....	13
	4.4.1. TIP/TILT/ROTATE SYSTEM.....	14
	4.4.2. EXTENDED SOURCE CAPABILITY .....	14
5.	MIRROR MODULE ASSEMBLIES (MMA).....	15
	5.1. MMA OVERVIEW .....	15
	5.2. MMA PERFORMANCE (GROUND CALIBRATION).....	15
	5.2.1. EFFECTIVE AREA .....	15
	5.2.2. ANGULAR RESOLUTION .....	17
	5.2.3. GHOST RAYS.....	19
	5.2.4. FOCAL LENGTH.....	20

<b>IXPE Science Operations Center</b>		
<b>Title: User Guide — Observatory</b>	<b>Document No.: IXPE-SOC-DOC-011</b>	<b>Revision: A</b>
	<b>Effective Date: 2022-07-22</b>	<b>Page: 5 of 69</b>

5.2.4.1.	DEFOCUSING ERROR .....	20
6.	INSTRUMENT.....	21
6.1.	INSTRUMENT OVERVIEW .....	21
6.2.	DETECTOR UNITS .....	21
6.2.1.	DESIGN .....	21
6.2.2.	DU PERFORMANCE.....	23
6.2.2.1.	QUANTUM EFFICIENCY .....	23
6.2.2.2.	ENERGY RESOLUTION.....	24
6.2.2.3.	SPATIAL RESOLUTION .....	25
6.2.2.4.	MODULATION FACTOR .....	25
6.2.2.5.	SPURIOUS MODULATION.....	26
6.2.2.6.	RATE-DEPENDENT GAIN VARIATIONS .....	27
6.2.2.7.	LONG-TERM FILL-GAS-PRESSURE VARIATION .....	27
6.2.2.8.	BACKGROUND.....	28
6.2.3.	FILTER/CALIBRATION WHEEL .....	28
6.3.	DETECTORS SERVICE UNIT (DSU).....	29
6.4.	INSTRUMENT OPERATION .....	30
6.4.1.	MODES OF OPERATION .....	30
6.4.2.	DEAD TIME / RATE CAPABILITY.....	32
6.4.3.	HOT PIXEL MASKING.....	32
6.4.4.	TIMING.....	32
6.5.	DATA ANALYSIS.....	33
6.5.1.	EVENT RECONSTRUCTION.....	33
6.5.2.	CALIBRATION AND REMOVAL OF SPURIOUS EFFECTS .....	36
6.5.3.	EVENT WEIGHTING .....	37
6.5.4.	DETECTOR RESPONSE AND HIGH-LEVEL SCIENCE ANALYSIS .....	38
7.	TELESCOPE PERFORMANCE (GROUND CALIBRATION).....	40
7.1.	ANGULAR RESOLUTION.....	40
7.1.1.	COMPARISON OF MEASURED TO PREDICTED TELESCOPE HALF POWER DIAMETER .....	43
7.2.	EFFECTIVE AREA.....	46

<b>IXPE Science Operations Center</b>		
<b>Title: User Guide — Observatory</b>	<b>Document No.: IXPE-SOC-DOC-011</b>	<b>Revision: A</b>
	<b>Effective Date: 2022-07-22</b>	<b>Page: 6 of 69</b>

7.2.1. COMPARISON OF MEASURED TO PREDICTED TELESCOPE EFFECTIVE AREA .....49

7.3. POLARIZATION RESPONSE .....52

7.3.1. MODULATION FACTOR .....52

7.3.2. SPURIOUS MODULATION.....53

8. APPENDIX A: EFFECTIVE-AREA CORRECTION FOR FINITE SOURCE DISTANCE .....56

9. APPENDIX B: MMA EFFECTIVE AREAS, CORRECTED FOR INIFINITE SOURCE DISTANCE .....59

10. APPENDIX C: ACRONYM LIST .....66

11. REFERENCES .....68

IXPE Science Operations Center		
Title: User Guide — Observatory	Document No.: IXPE-SOC-DOC-011	Revision: A
	Effective Date: 2022-07-22	Page: 7 of 69

## 1 MISSION OVERVIEW

The Imaging X-ray Polarimetry Explorer (IXPE) is a Small Explorer Mission designed to open a new window of investigation -- X-ray polarimetry. The IXPE observatory features 3 identical telescopes each consisting of a mirror module assembly with a polarization-sensitive imaging x-ray detector at its focus. An extending boom, deployed on orbit, provides the necessary 4 m focal length. The payload sits atop a 3-axis stabilized spacecraft which, among other things, provides power, attitude determination and control, commanding, and telemetry to the ground. During its 2-year baseline mission, IXPE will conduct precise polarimetry for samples of multiple categories of x-ray sources, with follow-on observations of selected targets.

The IXPE observatory was launched on a dedicated Falcon-9 rocket from Kennedy Space Center on Dec 9, 2021. It was inserted into an equatorial orbit with an apogee of 605.6 km and an inclination of 0.23°. This orbit inclination provides a low charged-particle background and allows frequent data downloads to the primary ground station in Malindi, Kenya (a backup ground station is in Singapore). The chosen altitude maximizes the orbit lifetime (projected to be 18 years) while still satisfying a NASA requirement of re-entry within 25 years.

The IXPE Mission is an international collaboration led by NASA Marshall Space Flight Center (MSFC) as the Principal Investigator (PI, Dr Martin Weisskopf) Institution and includes Ball Aerospace (Ball), University of Colorado / Laboratory for Atmospheric and Space Physics (CU/LASP), as well as the Italian Space Agency (ASI) with the IXPE Italian Team (I2T) consisting of Istituto di Astrofisica e Planetologia Spaziali / Istituto Nazionale di Astrofisica (IAPS/INAF), Istituto Nazionale di Fisica Nucleare (INFN) and OHB-I as major international partners.

NASA's Small Explorers are PI-led missions, with the PI team, program management, system engineering, and safety and mission assurance oversight all at MSFC. In addition, MSFC is responsible for the Mirror Module Assembly (MMA) fabrication, testing, and calibration, as well as for science operations and data analysis. Thermal shields for the MMAs are provided as a contribution by Nagoya University, Japan. Program partners at the Italian Space Agency (Agenzia Spaziale Italiana, ASI) provide funding for the polarization-sensitive detectors as well as the Malindi ground station and scientific support with its Space Science Data Center (SSDC). The IXPE spacecraft is provided by Ball Aerospace, which is also responsible for observatory integration and testing. Finally, to aid in science planning, IXPE has a large science advisory team, comprising of more than 100 scientists from 12 countries. Figure 1.1 shows the IXPE team and responsibilities.

IXPE Science Operations Center		
Title: User Guide — Observatory	Document No.: IXPE-SOC-DOC-011	Revision: A
	Effective Date: 2022-07-22	Page: 8 of 69



**Figure 1.1:** The IXPE team and responsibilities

## 2 GROUND SYSTEM

### 2.1 Overview

Communication with IXPE is via a primary ground station in Malindi, Kenya, with a backup station in Singapore. Data download will vary with observing program but will average around 7-8 contacts per day. Commanding will be approximately once per week.

Mission operations will be run from the Mission Operation Center (MOC) run by the Laboratory for Atmospheric and Space Physics (LASP) located at the University of Colorado. The MOC communicates with the Science Operations Center (SOC), at the Marshall Space Flight Center, sending data for processing, and with the observatory via the ground network shown in Figure 2.1. Data from the SOC are sent to the High Energy Astrophysics Science Archive Research Center (HEASARC) for archiving and public access.

IXPE Science Operations Center		
<b>Title: User Guide — Observatory</b>	<b>Document No.: IXPE-SOC-DOC-011</b>	<b>Revision: A</b>
	<b>Effective Date: 2022-07-22</b>	<b>Page: 9 of 69</b>

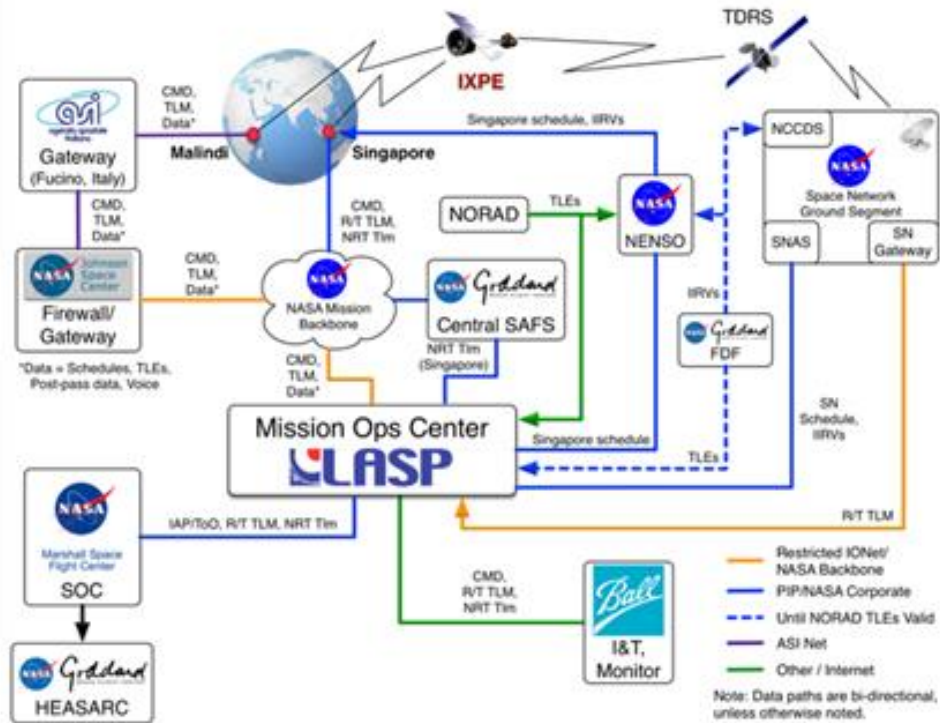


**Figure 2.1:** IXPE ground network

## 2.2 Downlink and Uplink Capability

IXPE uses S-band communication for both downlinking and uplinking. Downlink is at 2 Mbps, with a capacity of ~ 100 Mbytes for a single ground contact. An average 7-8 contacts per day is expected, although this can be increased for specific targets with high data rates (such as the Crab Nebula). An on-board solid-state recorder provides 6 GBytes of storage, thus the brightest targets will have their observations segmented with fainter targets to allow the recorder time to unload data.

## 2.3 Mission Operations Center (MOC)

The MOC is responsible for operating the Observatory—both spacecraft and payload, the former in close collaboration with Ball and MSFC, and the latter in close collaboration also with Italy. The MOC monitors the health and safety of the Observatory, uploads science target information once per week, and downloads science data. If communication passes are missed, the data (stored in on-board memory) are re-transmitted at the next available pass, so that no data are lost.

## 2.4 Science Operations Center (SOC)

The SOC is responsible for science operations. The SOC formulates the long-term observing plan that is then sent to the MOC for detailed scheduling on a weekly basis, so that targets of opportunity can be scheduled as they arise. The scheduling also includes planned insertions of the on-board calibration sources that are used for detector unit performance monitoring.

IXPE Science Operations Center		
Title: User Guide — Observatory	Document No.: IXPE-SOC-DOC-011	Revision: A
	Effective Date: 2022-07-22	Page: 10 of 69

The SOC receives all the observatory data, both science and engineering, which it then processes. Science data products are then distributed to the HEASARC for public access within 1 week after the end of an observation (after an initial 3-month checkout period during which the turnaround time is 30 days)

### 2.4.1 Data Products

These consist of the following:

- 1) Level-1 products, FITS files containing individual photoelectron tracks plus emission directions in detector co-ordinates
- 2) Level-2 products, event lists of processed tracks giving polarization information in sky co-ordinates
- 3) Low-level products produced for the Instrument Team to allow for health monitoring and long-term trending

### 2.4.2 Observation Schedule

A current version of the science-target observing schedule is given at

[https://ixpe.msfc.nasa.gov/for\\_scientists/ltp.html](https://ixpe.msfc.nasa.gov/for_scientists/ltp.html)

#### 2.4.2.1 Target Visibility

Given the Observatory 600 km orbit altitude, the amount of time a source is visible, per 95-minute orbit, is dependent upon its declination. Above an absolute declination value of  $67^\circ$  a source is never eclipsed by the earth. Conversely, the minimum observing time, for a source near the celestial equator is  $\sim 60$  mins per orbit. However, the equatorial orbit does clip the edge of the South Atlantic Anomaly, and so, as a conservative measure to prevent any possible gas pixel detector (section 6.2.1) damage, the detectors' high voltage is lowered for a period set by geographical location, amounting to approximately 10 minutes per orbit. For eclipsing targets, the SAA passage may sometimes when the target is already occulted, and so no additional signal loss is incurred.

#### 2.4.2.2 Targets of Opportunity

Targets of opportunity are requested via a form available at the MSFC IXPE site: <https://ixpe.msfc.nasa.gov>.

## 3 ATTITUDE DETERMINATION AND CONTROL

### 3.1 System

The IXPE ADCS system consists of sun sensors and a magnetometer for coarse aspect and a star tracker for fine aspect. Control is via 3 reaction wheels with 3 magnetic torquers to offload momentum.

IXPE Science Operations Center		
Title: User Guide — Observatory	Document No.: IXPE-SOC-DOC-011	Revision: A
	Effective Date: 2022-07-22	Page: 11 of 69

### 3.1.1 GPS Receiver

IXPE is equipped with a Surrey SGR-10 GPS system, which provides accuracies of 20-m orbital positions, 0.25-m/s orbital velocity, and 1- $\mu$ s timing.

### 3.1.2 Star Tracker

IXPE uses a SODERN Hydra-M star tracker system with two 22° field-of-view heads, one mounted to the mirror module support structure and facing forwards (+Z direction) and the other mounted at the rear of the spacecraft deck and facing aft. An electronics unit which interfaces to the tracker heads produces quaternions which are sent to the spacecraft computer (IAU). The system provides attitude which satisfies IXPE's requirement of placing an image on the celestial sphere to 12 arcsec ( $3\sigma$  per axis).

## 3.2 Slew Capability

The IXPE Observatory can slew 90 degrees in approximately 30 minutes.

## 4 PAYLOAD

The IXPE payload (Figure 4.1) consists of a deployable section containing three co-aligned mirror module assemblies and a star tracker mounted in a support structure with x-ray shields attached. Connecting this structure to the spacecraft is a deployable boom with a thermal sock which establishes the system focal length. Completing the payload are three detector units mounted on the top deck of the spacecraft and aligned with the mirror modules forming three identical x-ray telescopes. An additional tip/tilt/rotate system between the mirror module support structure and the boom permits on-orbit fine adjustment of telescope alignment.

### 4.1 Telescopes

The IXPE payload features 3 identical telescopes, each comprising Mirror Module Assembly with a Detector Unit (DU) at its focus. The DUs are clocked at 120 degrees to each other to help mitigate any systematic effects when the three sets of data are added. Each DU operates independently. A Detectors Service Unit (DSU) co-ordinates activities of the three DUs and merges the resulting data for transmission to the spacecraft computer (the Integrated Avionics Unit).

IXPE Science Operations Center		
Title: User Guide — Observatory	Document No.: IXPE-SOC-DOC-011	Revision: A
	Effective Date: 2022-07-22	Page: 12 of 69

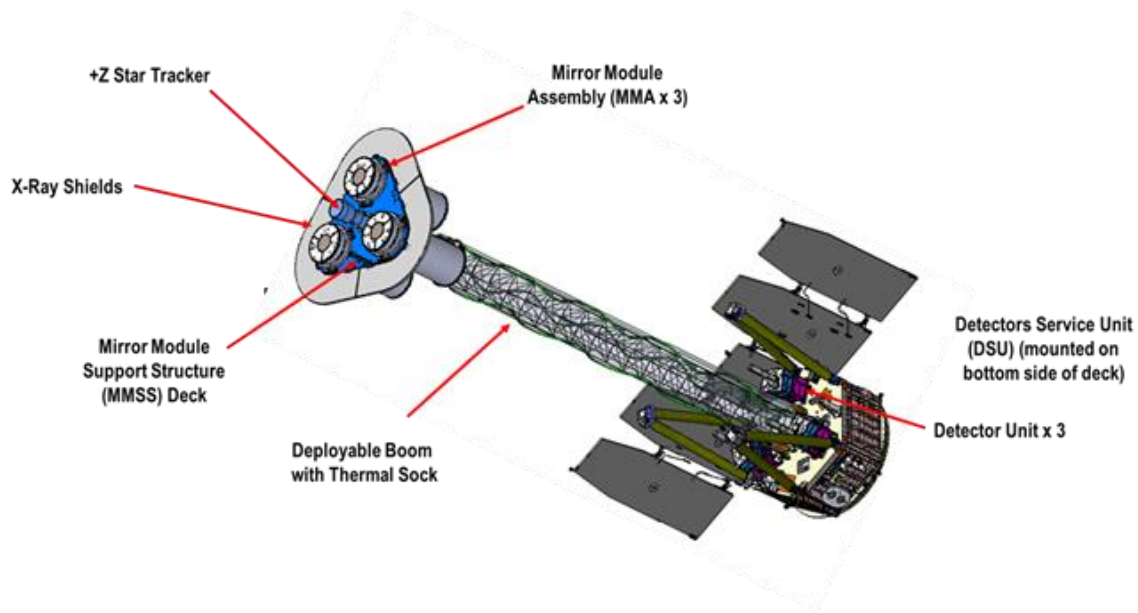


Figure 4.1: IXPE Observatory payload elements

## 4.2 IXPE Coilable Boom

To provide the necessary 4-m focal length, yet fit within the fairing of the original Pegasus launch vehicle, IXPE utilizes a coilable extending boom that deploys on orbit (see Figure 3). The boom, provided by Northrop Grumman Space Systems, is triangular in section, with three glass-fiber longerons that extend along its full length. Battens and diagonals complete the structure and provide additional stiffness when deployed.

The boom was initially coiled in a heated canister. Upon release, it uncoiled via stored strain energy in a controlled manner, using a lanyard and a damper to govern the deployment speed. On orbit, deployment took 2-3 minutes, after which it took another 2 mins for oscillations to dampen. During deployment, the boom uncoiled ~3.5 turns, to place the detectors below their respective detectors.

Covering the boom is a 2-layer Kapton thermal sock, which limits boom temperature excursions around the orbit thereby reducing shifts in the relative node positions of the optics to the detectors. Pre-launch estimates of diurnal motions of the MMA node relative to the detector node are 18 arcsec, worse case<sup>1</sup>.

## 4.3 X-ray Shields

Attached to the MMSS is an X-ray shield system that wraps around the outside of the three MMAs (see Figure 4.1). These shields work in conjunction with the collimator atop each DU, to prevent stray radiation that has not gone through the MMA from reaching the entrance window of the DU.

<sup>1</sup> IXPE deployed thermal distortion analysis, Ball Document No. 2513581.

IXPE Science Operations Center		
Title: User Guide — Observatory	Document No.: IXPE-SOC-DOC-011	Revision: A
	Effective Date: 2022-07-22	Page: 13 of 69

The shields are fabricated from aluminum honeycomb panels which provide an effective thickness of  $> 0.25$  mm, offering essentially 100% opacity over the IXPE energy range.

#### 4.4 Telescope Alignment

The IXPE focal plane detector has an active area of  $15\text{ mm} \times 15\text{ mm}$ , thus each telescope must be carefully aligned to ensure the image is near the center of the detector and that the axis of each mirror module is co-aligned with the star tracker. The driving requirement here is the capability to simultaneously place an extended source of diameter up to 9 arcminutes on all three detectors.

Alignment primarily consists of placing the three DUs and the three MMAs on congruent triangles, the former on the top deck of the spacecraft and the latter on the deployable mirror module support structure. Surface mount reflectors (SMRs) installed on the MMAs and DUs during construction enable this process which is done using a laser tracker system. Precise knowledge linking the SMR positions to the respective nodes of the MMAs and the DUs is derived to high precision ( $< 100\text{ }\mu\text{m}$ ) during component assembly. Before the MMAs are placed precisely in position, their x-ray axes are co-aligned with each other and with the optical axis of the forward star tracker using alignment cubes mounted on each MMA and measured during x-ray calibration (see Figure 4.2).

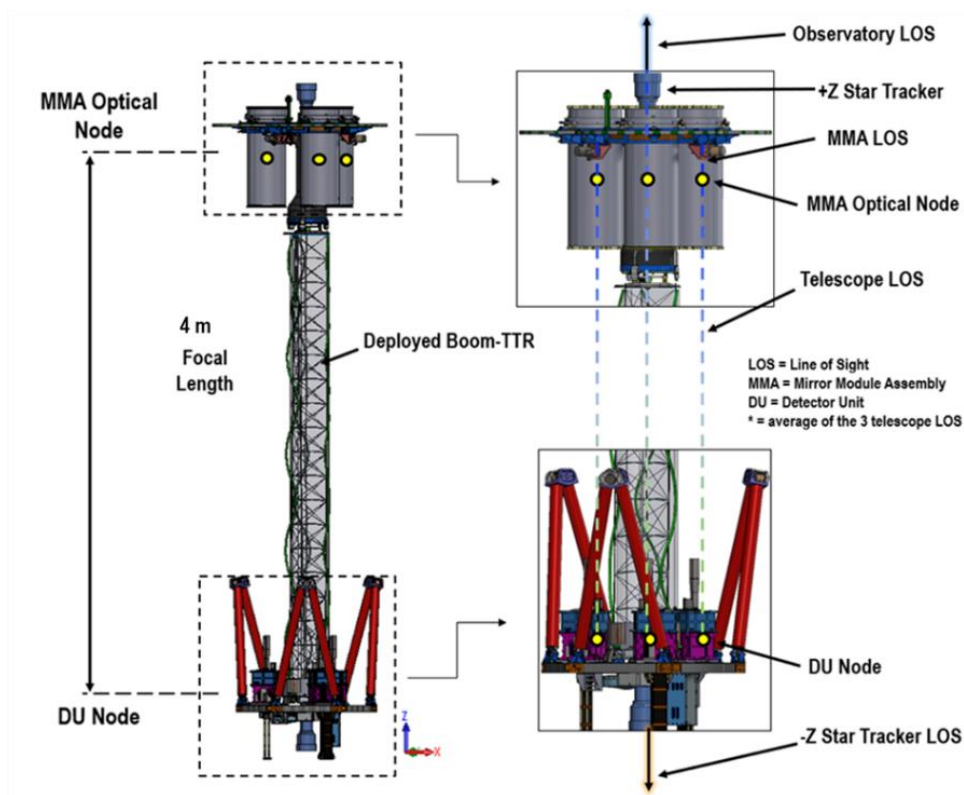


Figure 4.2: Telescope alignment schematic

IXPE Science Operations Center		
Title: User Guide — Observatory	Document No.: IXPE-SOC-DOC-011	Revision: A
	Effective Date: 2022-07-22	Page: 14 of 69

#### 4.4.1 Tip/Tilt/Rotate System

The deployment accuracy of the boom is such that the x-ray image of an on-axis x-ray source should be within  $\sim 1$  mm ( $1\text{-}\sigma$ ) of the center of each detector. For precise alignment, use may be made of an on-board Tip/Tilt/Rotate (TTR) system (Figure 4.3, left). Situated between the boom and the mirror module support structure, the TTR can effectively re-point the observatory to move the image on the detector as shown in Figure 4.3 (right). This is possible because the star tracker is mounted on the MMSS, so that adjusting the TTR in tip/tilt has the effect of offset point the observatory which then moves to re-acquire the target. The rotate component of the TTR compensates for any rotational offset when the boom deploys.

The TTR range is approximately  $\pm 0.15$  degrees in tip and tilt and  $\pm 2.6$  degrees in rotation. The motion afforded by this was designed to be an order of magnitude larger than any deployment tolerances. It is expected that the TTR will be used a small number of times throughout the life of the mission.

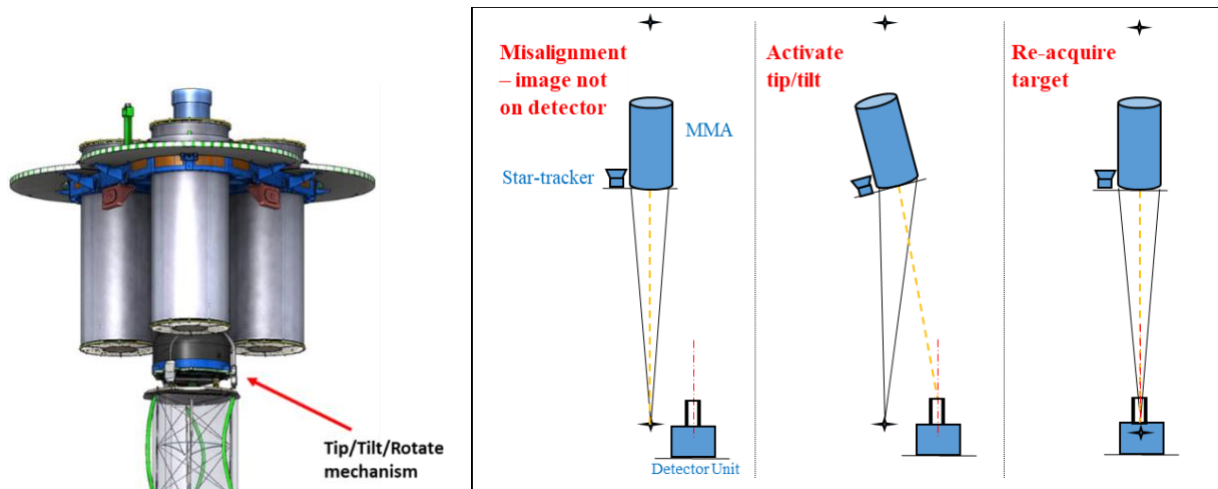


**Figure 4.3:** Left image shows the Tip/Tilt/Rotate mechanism; Right drawing shows the telescope on-orbit alignment scheme

#### 4.4.2 Extended Source Capability

The Level-1 requirement to be able to image a 9-arcmin-diameter target simultaneously in all three telescopes places requirements on both telescope co-alignments and on pointing accuracy. Each DU has a requirement for at least an 11-arcmin-diameter field of view with full track recognition (equivalent to  $\sim 13$  mm diameter) and so that leaves 1 arcminute to be allocated to pointing an alignment. At launch, the best estimate of these were 24.7 arcsec for pointing and 27.5 arcsec for alignment ( $3\sigma$ ). Thus, a system-level field of view of 9.8 arcmin is predicted with 99% confidence.

IXPE Science Operations Center		
Title: User Guide — Observatory	Document No.: IXPE-SOC-DOC-011	Revision: A
	Effective Date: 2022-07-22	Page: 15 of 69

## 5 MIRROR MODULE ASSEMBLIES (MMA)

### 5.1 MMA Overview

The IXPE payload is comprised of three identical mirror module assemblies, each containing 24 concentrically-nested nickel/cobalt mirror shells. The shells range in diameter from ~ 160 mm to 270 mm and each is a cylindrical structure 600 mm long that contains both parabolic and hyperbolic segments of the Wolter-1 geometry<sup>1</sup>. The mirror shells are uncoated, the NiCo substrate material giving good reflectivity in IXPE’s energy range of 2-8 keV. Table 5.1 gives the parameters of the MMAs.

Parameter	Value
Number of mirror modules	3
Number of shells per mirror module	24
Focal length	4 m
Total shell length	600 mm
Range of shell diameters	162–272 mm
Range of shell thicknesses	0.18–0.25 mm
Shell material	Electroformed nickel–cobalt alloy
Effective area per mirror module	166 cm <sup>2</sup> (@ 2.3 keV); > 175 cm <sup>2</sup> (3–6 keV)
Angular resolution (HPD)	≤ 28 arcsec
Field of view (detector limited)	12.9 arcmin square

**Table 5.1:** Mirror Module Assembly (MMA) parameters

### 5.2 MMA Performance (Ground Calibration)

The four IXPE MMAs (3 flight unit plus one spare) were calibrated in the MSFC Stray Light Test Facility (SLTF) from 7/17/2020 through 1/20/2021. The calibration data were intended to provide a database for scientific data analysis during the mission. For additional information on MMA calibration see IXPE-RPT-180, baseline, dated 4/12/2021.

#### 5.2.1 Effective Area

During calibration at the MSFC Stray Light Test Facility (SLTF), x-ray sources of characteristic line energies 2.3 keV (Molybdenum L), 4.5 keV (Titanium K<sub>α</sub>) and 6.4 keV (Iron K<sub>α</sub>) illuminate the MMA under test, which in turn focuses the flux onto a silicon drift detector (SDD). Simultaneously, the source illuminates an identical and cross-calibrated (Beam Monitor) SDD placed near the MMA entrance aperture. Due to the nature of the x-ray sources and the source settings, this approach measures both a continuum effective area covering the IXPE bandpass and, with better statistics, line effective areas at the energies of the x-ray source lines. The line effective areas measured at 2.3, 4.5 and 6.4 keV are shown in the tables below. NB: A pulse-height region of interest was selected to isolate Ti-K<sub>α</sub> (4.51 keV) from K<sub>β</sub> (4.93 keV) and Fe-K<sub>α</sub> (6.4 keV) from Fe-K<sub>β</sub> (7.0 keV).

IXPE Science Operations Center		
Title: User Guide — Observatory	Document No.: IXPE-SOC-DOC-011	Revision: A
	Effective Date: 2022-07-22	Page: 16 of 69

The ratio of focused to unfocused count rates, multiplied by the known active area ( $50 \text{ mm}^2$ ), of the SDD, gives directly the effective area of the MMA at the finite-source (object) distance of 97.950 meters (from the x-ray source to the MMA node as installed at SLTF). An analytical correction is applied to the finite-source-distance effective area to give the on-orbit infinite-source-distance effective area. This correction has been verified experimentally and by a ray-trace analysis of the IXPE optics. Effective area data were taken on-axis and at 16 off-axis angles at each of 4 azimuths.

The derived on-axis effective area at the characteristic line energies is shown in Table 5.2. The continuum on-axis effective area for the three flight modules is shown in Figure 5.1.

Mirror Module Assembly	2.3 keV	4.5 keV
MMA1	168 $\text{cm}^2$	195 $\text{cm}^2$
MMA2	167 $\text{cm}^2$	195 $\text{cm}^2$
MMA3	167 $\text{cm}^2$	200 $\text{cm}^2$

**Table 5.2:** Flight MMA on-axis effective areas at given line energies corrected for infinite source distance

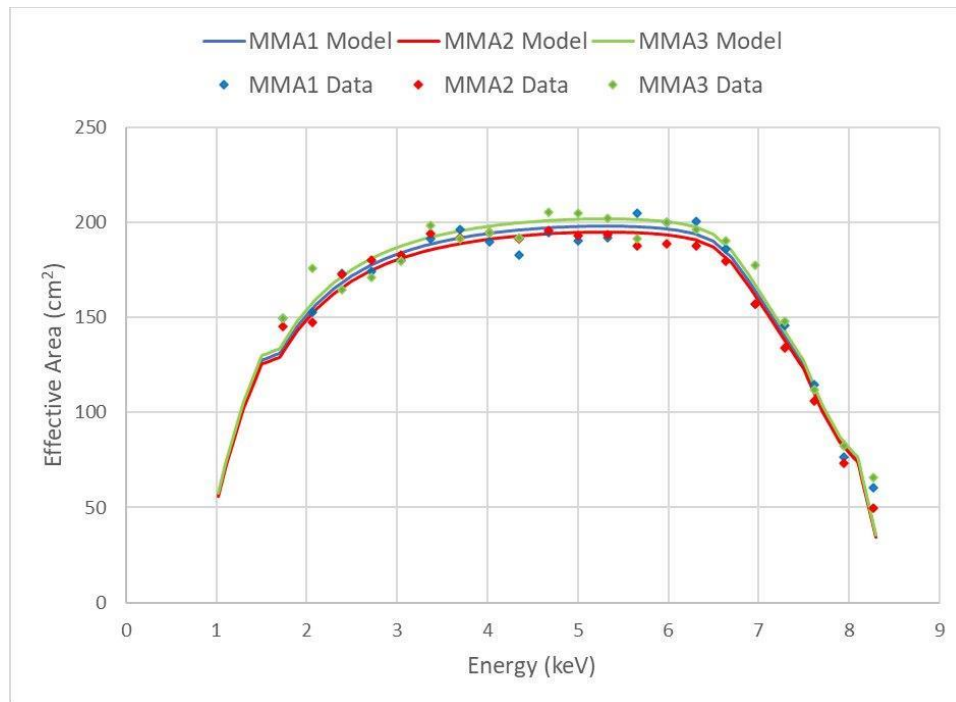
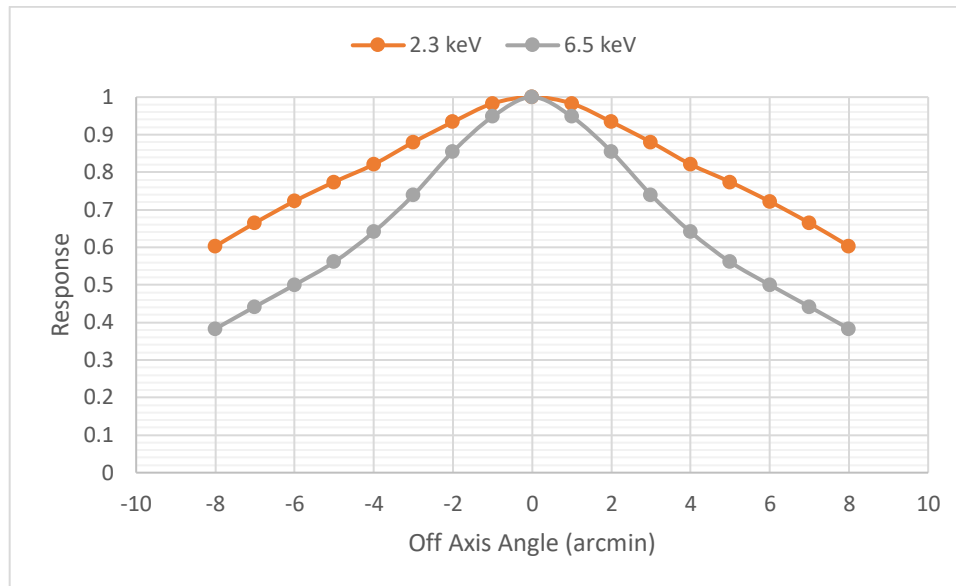


Figure 5.1: Continuum on-axis effective area for the flight MMAs corrected to infinite source distance. Solid line represents best-fit model

The best fit data, from the models in Figure 5.1, are given in Appendix B for in 0.04-keV increments. Data were also taken for several off-axis angles. A typical vignetting function, derived from calibration of MMA 1 and corrected for infinite source distance, is shown in Figure 5.2.

IXPE Science Operations Center		
Title: User Guide — Observatory	Document No.: IXPE-SOC-DOC-011	Revision: A
	Effective Date: 2022-07-22	Page: 17 of 69



**Figure 5.2:** Vignetting function measured at 2 energies for MMA 1

## 5.2.2 Angular Resolution

For each MMA, a focused image was taken at Mo  $L\alpha$  (2.29 keV) and Titanium  $K\alpha$  (4.5 keV) using the ANDOR CCD camera (0.7 arcsec/pixel), as per IXPE calibration procedure IXPE-CAL-163 (baseline), section 7.2. The CCD-camera data were then used to generate an encircled energy plot and identify the radius containing 50% of the measured flux, which is doubled to obtain the Half Power Diameter (HPD). The procedure outlined below, defines the process in greater detail:

1. Add all appropriate source images called out in Cal-163 to give an average image frame
2. Process flat-field images called out in Cal-163 by removing the largest and smallest pixels (in terms of total counts) and taking the average of the rest
3. Subtract the resulting flat field from the resulting image frame
4. Correct the flat-field subtraction a second time to get the noise peak centered on zero. Also, remove cosmic rays and other artifacts.
5. Remove smearing if necessary
6. Using a 25-arcsec-diameter circle (the approximate expected HPD), check image for largest number of integrated counts (i.e., find the center of the source)
7. Calculate the radii (in arc seconds) of all the pixels from this center. Order them according to counts to get a cumulative count distribution out to 4 mm radius
8. Take 50% cumulative count point to give the half-power radius and double this to get the HPD

Figures 5.3, 5.4 and 5.5 show some typical on-axis data obtained for each flight MMA.

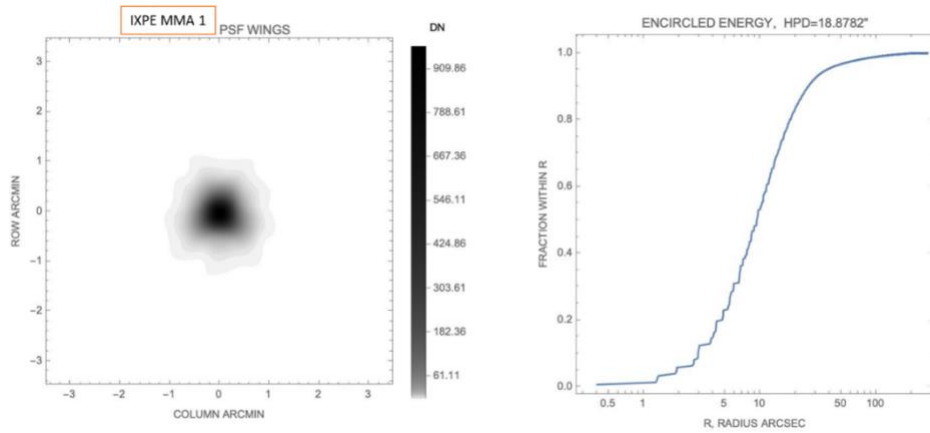


**Figure 5.3:** Image contour plot and encircled energy distribution for MMA1 at 4.5 keV

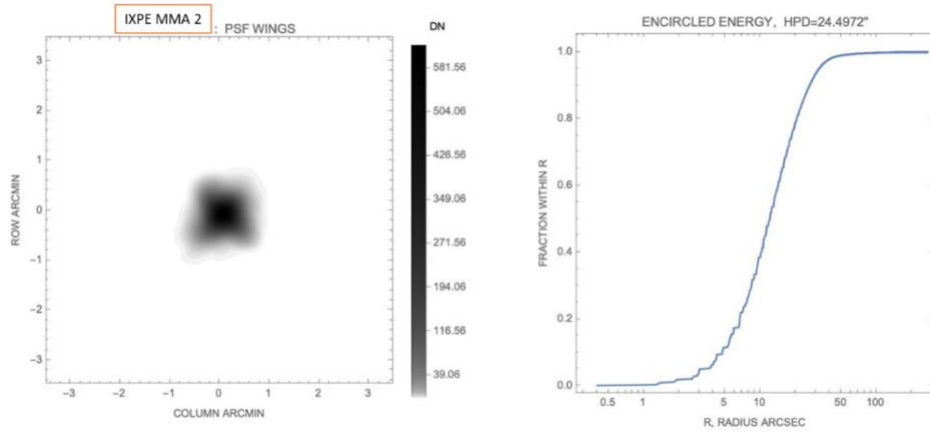


**Figure 5.4:** Image contour plot and encircled energy distribution for MMA2 at 2.3 keV

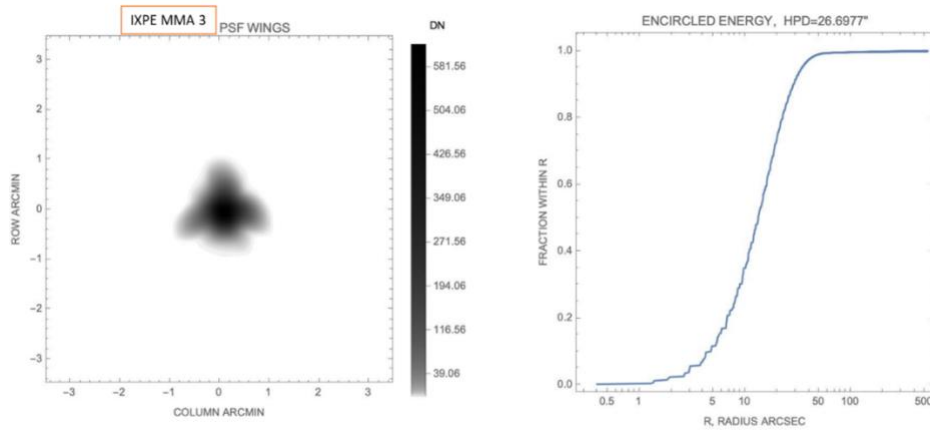


**Figure 5.5:** Image contour plot and encircled energy distribution for MMA3 at 2.3 keV

IXPE Science Operations Center		
Title: User Guide — Observatory	Document No.: IXPE-SOC-DOC-011	Revision: A
	Effective Date: 2022-07-22	Page: 19 of 69

Table 5.3 (below) displays the resulting HPD measurements for each flight plus spare MMA, at each energy. The 1- $\sigma$  errors on these numbers are estimated to be  $\pm 0.4$  arcsec.

		MMA1		MMA2		MMA3	
	Energy (keV)	2.3	4.5	2.3	4.5	2.3	4.5
At Focus	HPD (arcsec)	19.0	19.9	25.0	26.0	27.6	28.0

**Table 5.3:** Measured Half-Power Diameter at 2.3 keV and 4.5 keV for MMA1, 2, and 3.

### 5.2.3 Ghost Rays

Ghost rays are from sources outside of the normal field of view which undergo a single reflection (instead of two) typically off the hyperbolic mirror segment and end up in the flight detector thereby contributing an additional background component. For point source measurements these are not an issue; for weak extended sources, where there are very bright point sources just outside of the field of view, this can potentially degrade the telescope sensitivity. IXPE has requirements on the amount of such stray radiation, controlled by heavily nesting the mirror shells to block off radiation paths, and verified as part of the x-ray calibration. The requirement calls for the flux from any source outside of the field of view to be reduced by at least a factor of 100 over what that source would be on axis. This requirement is driven by a planned observation of molecular clouds near the Galactic Center that are a weak source of x rays but have bright x-ray sources nearby just out of the field of view. Simulations show that above 1 degree off axis it is not possible for singly-reflected rays to reach the focal plane. Therefore, during calibration, data were taken at 2.3 keV up to and including this off-axis angle.

The process is straightforward. The optic is pitched or yawed to the appropriate off-axis angle, and the total number of counts in a 12.8-mm-diameter circle (equivalent to 11 arcminutes) centered on the MMA x-ray axis is registered. This number of counts is then divided into the number of counts for 0° off-axis angle (not shown) to obtain a reduction ratio.

Table 5.4 gives the reduction ratio for each MMA, as a function of off-axis angle, at 2.3 keV.

#### MMA1

Off-axis Angle	0.2°	0.4°	0.6°	0.8°	1.0°
Azimuth = 0°	280	735	872	1381	1780
Azimuth = 90°	241	595	858	897	650

#### MMA2

Off-axis Angle	0.2°	0.4°	0.6°	0.8°	1.0°
Azimuth = 0°	229	712	890	1160	1517
Azimuth = 90°	237	508	818	834	529

#### MMA3

Off-axis Angle	0.2°	0.4°	0.6°	0.8°	1.0°
Azimuth = 0°	262	776	770	1533	1543
Azimuth = 90°	221	510	981	796	681

**Table 5.4:** Measured ghost-ray attenuation as a function of off-axis angle

IXPE Science Operations Center		
Title: User Guide — Observatory	Document No.: IXPE-SOC-DOC-011	Revision: A
	Effective Date: 2022-07-22	Page: 20 of 69

## 5.2.4 Focal length

The focal length of each MMA is measured during calibration. The positions of the MMA and the CCD camera are measured with a Leica Laser Tracker system, to a nominal precision better than 0.001 inch (25  $\mu\text{m}$ ). The measurement is taken directly after x-ray calibration to ensure that the optic and detector are focused and aligned. The distance between the optic and detector (and hence the focal length of the optic) follows directly from the MMA and detector positions.

The Laser Tracker measurements yield the finite-source-distance focal length (for an x-ray source 97.950 meters from the node of the x-ray optic). The finite-distance focal length (image distance) is combined with the beamline distance (object distance) using the thin lens equation to give the on-orbit infinite-source-distance focal length. This approach has been verified using several ray-trace analyses by members of the team. The value referred to as the ‘focal length’ in the results Table 7 below is the infinite-source-distance value appropriate for flight. See Appendix A for more details.

Table 5.5 lists the resulting infinite-source-distance focal lengths.

MMA	Focal Length
MMA1	3997.2 mm
MMA2	3997.8 mm
MMA3	3997.6 mm

**Table 5.5:** The measured IXPE MMA focal lengths

The statistical uncertainty on the measurement is 0.6 mm (1- $\sigma$ ), based upon multiple measurements of the focal length of MMA3.

### 5.2.4.1 Defocusing Error (resolution expected on orbit)

As the IXPE payload was designed for a 4001 mm-focal-length system, it is evident that there is a few (3-4) mm shortfall in the flight MMAs. This shortfall leads to a slight defocusing of a telescope (MMA+DU), which effects a small increase in the MMA half-power diameter (HPD). Other factors that already affect the overall angular resolution are the native MMA angular resolution, the detector gas depth (10 mm), the detector spatial resolution, and the accuracy of the MMA-to-DU separation on the observatory.

Table 5.6 shows the measured MMA HPDs for MMAs 1, 2 and 3, at 3 energies. Succeeding lines in the table add the effects on the HPD of the thick (10 mm) detector gas cell (which further defocusses the beam) and the measured spatial resolution of the detector (see section 6.2.2.3); the accuracy of the aspect system; the focal-length uncertainty stemming from observatory assembly (a max separation of DU and MMA of 4001.65 mm)); and an MMA focal length 4 mm too short. The bottom filled line in the table gives the effective HPD of each telescope in this worst-case scenario—i.e., assuming that the observatory assembly uncertainty adds to the 4-mm focal-length mismatch. This gives the best estimate, pre-launch, of the expected on-orbit angular resolution of each telescope.

IXPE Science Operations Center		
Title: User Guide — Observatory	Document No.: IXPE-SOC-DOC-011	Revision: A
	Effective Date: 2022-07-22	Page: 21 of 69

	MMA1		MMA2		MMA3	
Energy (keV)	2.3	4.5	2.3	4.5	2.3	4.5
Native MMA resolution (arcsec HPD)	19.0	19.9	25.0	26.0	27.6	28.0
Add in detector effects (arcsec HPD)	21.4	22.5	27.0	28.2	29.2	29.8
Add in defocus + aspect (arcsec HPD)	24.0	24.8	28.5	29.3	30.0	30.2

**Table 5.6:** Estimate of on-orbit telescope angular resolution (see text)

## 6 INSTRUMENT

### 6.1 Instrument Overview

The IXPE instrument is an Italian contribution funded by the Italian Space Agency (ASI) through the Istituto di Astrofisica e Planetologia Spaziali (IAPS) and the Istituto Nazionale di Fisica Nucleare (INFN). It comprises three flight Detector Units (DU) and a single Detectors Service Unit (DSU). The DUs each contain a gas pixel detector, which is essentially the heart of the instrument. Inside the GPD is a gas cell, holding the detection medium, and a custom ASIC to read the signals out. The DU also contains the back-end electronics which process the data and a filter and calibration wheel assembly (FCW). The DSU provides the three DUs with the required power, controls the FCW, and formats the scientific data and forwards it to the spacecraft computer for storage and eventual transmission to the ground.

### 6.2 Detector Units

#### 6.2.1 Design

The heart of the IXPE payload are the detector units (DUs). Located at the focus of each MMA these provide position sensitivity, energy determination, timing information and, most importantly, polarization sensitivity. Inside each DU is a Gas Pixel Detector<sup>2,3,4</sup> (GPD) which images the photoelectron tracks produced by x rays absorbed in the special fill gas (Dimethyl Ether - DME). The initial emission direction of the photoelectron contains the necessary information to determine the polarization of the source, while the initial interaction point and the total charge in the track provide the location and energy of the absorbed x ray, respectively.

Figure 6.1 shows a schematic of the GPD. An x ray enters through a beryllium window and interacts in the DME fill gas. The resulting photoelectron leaves a trail of ionization, and this photoelectron track drifts through a Gas Electron Multiplier (GEM), to provide charge gain, and onto a pixel anode readout. Table 6.1 gives the relevant performance parameters.

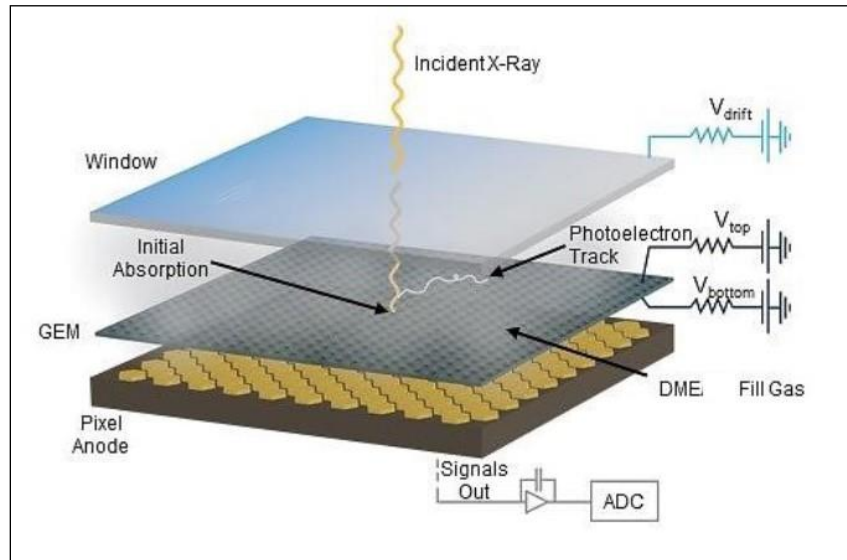


**Figure 6.1:** Schematic of the Gas Pixel Detector (GPD)

Parameter	Value
Sensitive area	15 mm × 15 mm (13 × 13 arcmin)
ASIC readout pitch	50 μm
Fill gas and asymptotic pressure	DME @ ~ 650 mbar
Detector window	50-μm thick beryllium
Absorption and drift region depth	10 mm
Spatial resolution (FWHM)	≤ 123 μm (6.4 arcsec) @ 2 keV
Energy resolution (FWHM)	0.57 keV @ 2 keV ( $\propto \sqrt{E}$ )
Useful energy range	2 - 8 keV

**Table 6.1:** Performance parameters of an IXPE Detector Unit (DU)

An expanded view of a detector unit is shown in Figure 6.2 (left). As well as the GPD, the unit houses all the back-end electronics to process each event, as well as high-voltage power supplies. It also houses a filter and calibration wheel assembly for on-orbit calibration, as well as a collimator for reduction of x-ray background. At the base of the collimator is a UV/ion shield used to prevent secondary emission from the GPD. Figure 6.2 (right) shows a photograph of a completed flight DU.

IXPE Science Operations Center		
Title: User Guide — Observatory	Document No.: IXPE-SOC-DOC-011	Revision: A
	Effective Date: 2022-07-22	Page: 23 of 69

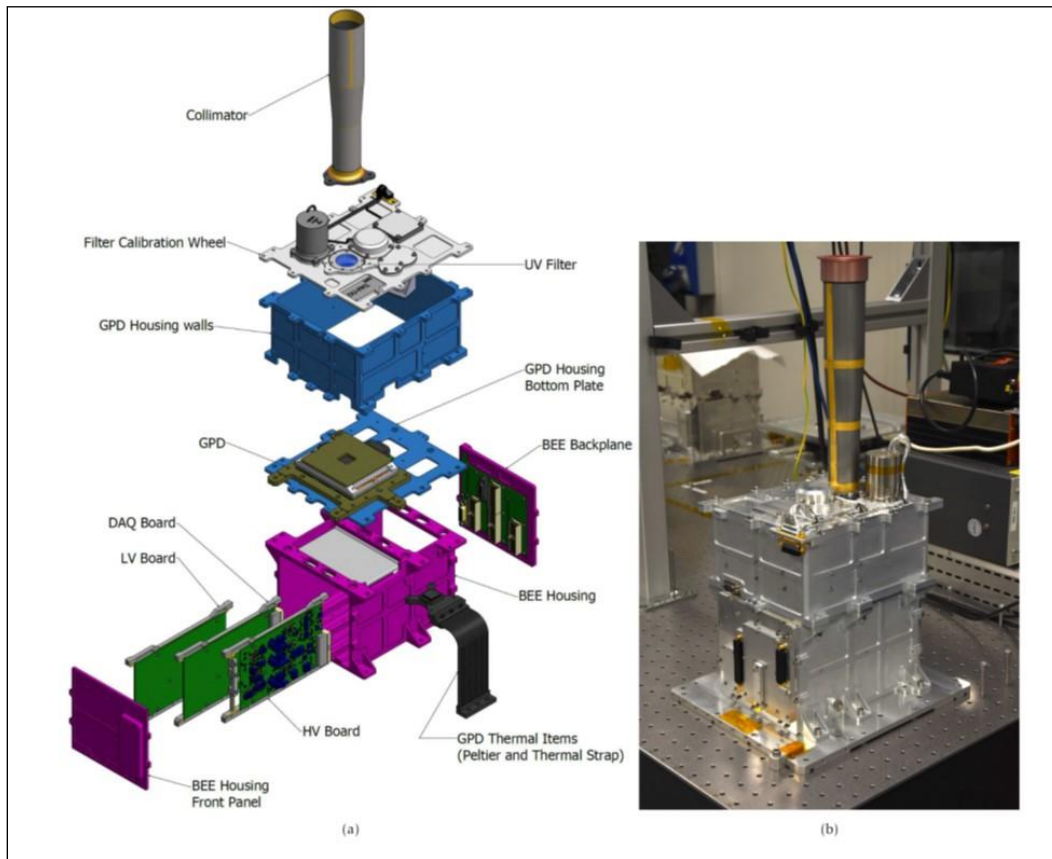


**Figure 6.2:** Expanded view of a Detector Unit (DU, left); photograph of a completed flight unit (right).

## 6.2.2 DU Performance

### 6.2.2.1 Quantum Efficiency

The efficiency of the DU is the product of the quantum efficiency of the GPD and the x-ray transmission of the ion-UV filter. It was measured during calibration at INAF-IAPS for each DU.

The x-ray transmission of the ion-UV filter was measured for all the flight units and agrees with the expected value for 1.06  $\mu\text{m}$  of Kapton coated with aluminum (50 nm) and carbon (5 nm).

The quantum efficiency of the GPD depends substantially on the DME pressure and depth, as well as the thickness of the beryllium window. The absorption gap is measured with high precision, as is the initial gas-fill pressure, but the fill-gas pressure has been found to change with time and so has been carefully modeled to predict the pressure at launch. The resulting DU quantum efficiency reached at launch is shown in Table 6.2, below.

IXPE Science Operations Center		
Title: User Guide — Observatory	Document No.: IXPE-SOC-DOC-011	Revision: A
	Effective Date: 2022-07-22	Page: 24 of 69

Detector FM#	Energy (keV)	Efficiency at Launch (%)
DU1	2.697	13.7
	6.400	1.77
DU2	2.697	13.4
	6.400	1.72
DU3	2.697	13.5
	6.400	1.74

**Table 6.2:** DU quantum efficiency at launch date

Each DU also has an attenuating (gray) filter as part of its filter/calibration set. The x-ray transmission of these filters have been measured at different energies and agree with the theoretical value expected for the 76- $\mu\text{m}$  Kapton foil. Measured transmission results at two energies are given in Table 6.3.

Detector FM#	Energy (keV)	Transmission (%)
DU1	2.697	17.2 $\pm$ 0.2
	6.400	87.7 $\pm$ 0.5
DU2	2.697	18.1 $\pm$ 0.2
	6.400	88.4 $\pm$ 0.6
DU3	2.697	17.0 $\pm$ 0.2
	6.400	88.0 $\pm$ 0.8

**Table 6.3:** Gray filter x-ray transmission.

### 6.2.2.2 Energy Resolution

Flat-field data obtained with the polarized sources were used to measure the energy resolution of each DU. This was done as the use of Bragg crystals in these sources renders the emission highly monochromatic. Spectral data were taken in 100 spots of 500- $\mu\text{m}$  radius from the flat field. The energy resolution was then calculated by fitting with a Gaussian the gain-corrected energy spectrum and dividing the measured FWHM by its peak. The energy resolution as a function of energy for the three flight DUs is shown in Figure 6.3.

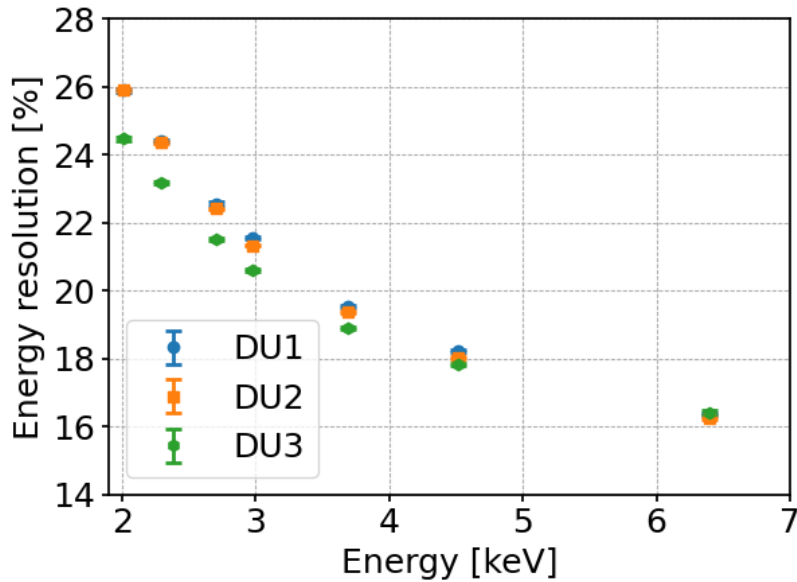


**Figure 6.3:** Energy resolution as a function of energy for the three flight DUs

### 6.2.2.3 Spatial Resolution

During ground calibrations the intrinsic spatial resolution has been estimated by measuring the Half Power Diameter using a beam on-axis with diameter less than 39 micrometers (measured by a CCD test detector). Measurements have been performed for both polarized and unpolarized sources and in different points across the sensitive area of the detectors. Details of these measurements are given in a dedicated paper in preparation (Di Marco A. et al. *Measurement of the spatial resolution of the IXPE Detector Units*). Table 6.4 shows the mean results taken for the 3 flight detector units.

Energy (keV)	HPD ( $\mu\text{m}$ )
2.70	$116.28 \pm 0.09$
6.40	$123.5 \pm 0.4$

**Table 6.4:** Mean spatial resolution of IXPE flight DUs as a function of energy.

### 6.2.2.4 Modulation Factor

The modulation factor was measured at different energies and polarization angles. This provides a check that the spurious modulation (section 1.2.5) was properly subtracted. A change of the modulation factor with polarization position angle would be expected in the presence of spurious effects, which mimic the presence of a secondary, albeit small, polarization component, and so these must be carefully removed. The net results from these measurements show that the modulation factor of the IXPE flight detectors is uniform over the detector sensitive surface and it is not dependent on polarization angle, providing evidence for correct spurious modulation removal. Calibration data have been analyzed subtracting spurious modulation using a specially derived algorithm<sup>5</sup> coupled with an optimum weighting approach<sup>6</sup>. From these data it is possible,

IXPE Science Operations Center		
Title: User Guide — Observatory	Document No.: IXPE-SOC-DOC-011	Revision: A
	Effective Date: 2022-07-22	Page: 26 of 69

considering the GPD secular pressure variation, section 6.2.2.7, to estimate the modulation factor as a function for the time of launch, as shown in Figure 6.4.

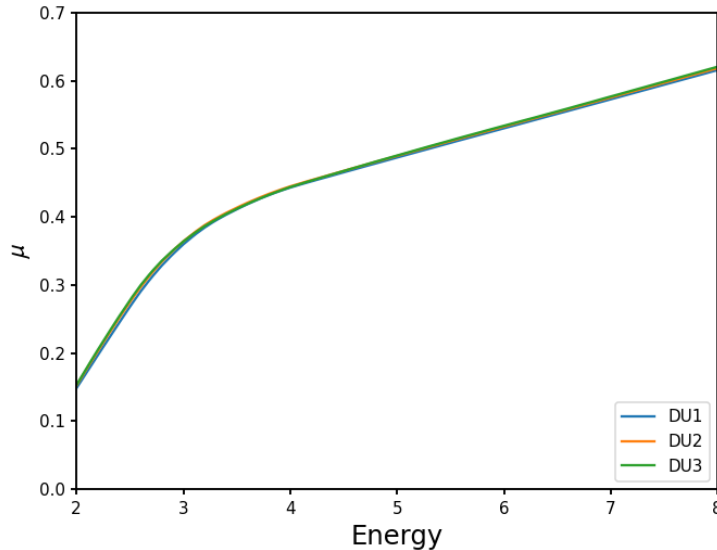


**Figure 6.4:** Modulation factor as function of energy for the IXPE flight DUs estimated at time of launch

### 6.2.2.5 Spurious Modulation

The response of an ideal polarimeter to unpolarized radiation is statistically flat. However, IXPE focal plane detectors show, especially at low energy, a nearly- $\cos^2$  modulation which indicates the presence of a low-level spurious signal. Although the root causes of such spurious polarization have been thoroughly investigated<sup>4</sup> the effect is hard to model and therefore was calibrated in detail. The response of each DU was measured at six energies with a flat illumination over the entire field of view, and with higher statistics in its center where the brightest sources will be observed<sup>7</sup>.

The spurious modulation amplitude expressed by Stokes parameters is shown in Figure 6.5. In the plot, the contributions from the three IXPE DUs are summed accounting for the clocking at  $120^\circ$  and normalized by the corresponding modulation factor. Spurious modulation has been verified to be constant with temperature and rate using GPD prototypes constructed during IXPE development. A small time dependence has been observed, due to variation with time of the GPD internal pressure. Such a variation, calculated for the pressure change from the calibration to the launch, is compliant with the requirement on the knowledge of spurious modulation, which is 0.3%<sup>7</sup>.

Spurious polarization will be removed event-by-event with an algorithm developed for this purpose<sup>8</sup>, allowing the end-user to treat data essentially as those obtained from an ideal polarimeter.

IXPE Science Operations Center		
Title: User Guide — Observatory	Document No.: IXPE-SOC-DOC-011	Revision: A
	Effective Date: 2022-07-22	Page: 27 of 69

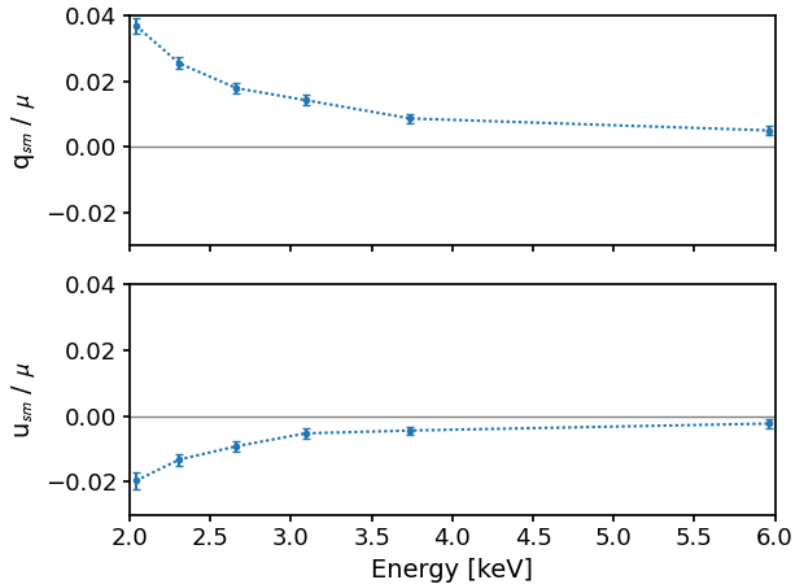


**Figure 6.5:** Stokes parameters of spurious polarization as a function of energy of the IXPE detectors. The effect is removed during the on-ground data processing

### 6.2.2.6 Rate-Dependent Gain Variations

The fine pitch of the IXPE GEMs makes them susceptible to rate-dependent gain variations due to temporary charge build-up. When the detector is irradiated, part of the charge from the avalanche can be temporarily deposited onto the dielectric substrate in the GEM holes, affecting the configuration of the electric field, and causing local (and reversible) changes in the gas gain. Since the charge trapping is not permanent, a competing discharging process is continuously at play, causing the gain to drift toward the initial value when the input energy flux is low enough.

Although this effect was largely mitigated by a dedicated fine tuning of the production process in the development stage of the mission, it is still present at a level that needs to be corrected for an accurate estimate of the energy and, since the modulation factor is energy-dependent, to correctly infer the source polarization from the measured modulation. For a typical x-ray celestial source, the effect will be of the order of a few %, on timescales of several hours to a day. For very bright sources we anticipate gain variations up to 10% on much shorter timescales.

To this end, we have developed a complete phenomenological model that allows us to measure and correct such gain variations dynamically, based on the energy flux measured by the GPD as a function of time and position across the active surface. (We emphasize that all the necessary information is included in the science data that are collected during normal observations, and that the onboard calibration sources can be used to ensure that there are no systematic drifts over long observations.) More details are provided in the referenced publication<sup>4</sup>.

### 6.2.2.7 Long-Term Fill-Gas-Pressure Variation

Through the development of the IXPE instrument it was realized that the internal gas pressure was undergoing a long-term decrease, over timescales of months, levelling out to an overall deficit of

IXPE Science Operations Center		
Title: User Guide — Observatory	Document No.: IXPE-SOC-DOC-011	Revision: A
	Effective Date: 2022-07-22	Page: 28 of 69

about 150 mbar (to be compared with the nominal 800 mbar at filling time). This observation, initially hinted by a slow increase of the gas gain, has since been confirmed by several indirect evidence (including the evolution of the quantum efficiency and the average track length at a given energy), as well as direct metrological measurements of the vertical displacement of the thin Be window.

The effect has been systematically monitored using a dozen (nominally identical) detectors, with test data amounting to more than 30 GPD-years equivalent of operation. Monitoring of the energy resolution has shown no change with time, clearly indicating that no leaks are involved (and in fact the detectors are filled to less than 1 bar, so a leak would increase pressure). The cause is most likely connected to adsorption phenomena within the cell itself. The pressure decrease is unambiguously saturating with time, and in fact for the three detectors installed on IXPE are all already within a few % of the expected asymptotic value. The current rate of change, typically of the order of a 1–10 mbar per year, is a generous upper limit to additional variations that we might expect on orbit. Onboard calibration sources allow monitoring of the detector evolution throughout the mission, by measuring the counting rate and the average track length.

Calibration data and simulations indicate that the impact of this pressure variation on the polarimetric sensitivity is mild. While the detector quantum efficiency scales linearly with the pressure, causing a net loss of effective area, the modulation factor increases as the pressure decreases, owing to fact that the tracks become more elongated. The net effect of these two competing processes is that the relative loss of sensitivity, expressed as the broadband minimum detectable polarization for a typical source spectrum, is less than 2% when going from the nominal 800 mbar to the actual 650 mbar.

#### 6.2.2.8 Background

The expected IXPE detector background has been modeled, taking into account the whole spacecraft and detailing the detector geometries<sup>9</sup>. This assessment considers all the major components of background such as the cosmic x-ray background, albedo Gamma, and albedo neutrons, primary electron, positron, protons and alpha, secondary electron, positron, and neutron. The expected counting rate from this assessment, without any background rejection, is  $4.7 \times 10^{-2}$  c/s/cm<sup>2</sup>/DU over 2-8 keV, and with rejection the net rate is  $1.16 \times 10^{-3}$  c/s/cm<sup>2</sup>/DU. The major contribution of un-rejected background are delta-rays from electron and positrons which are undistinguishable from source photo-electron tracks.

This level of background, approximately equal to 2  $\mu$ Crab, is obviously negligible for any point sources (polarimetry is in fact photon starved and typically possible only with the brighter sources for each class). It is also negligible for most extended sources which have high surface brightness. Only 1 weak extended source, molecular clouds near the Galactic Center, may have fluxes comparable to the background. However, the slight (few %) loss of polarization sensitivity caused by this will not be of concern as the expected level of polarization for this source is very high.

#### 6.2.3 Filter/Calibration Wheel

To enable in-flight calibration monitoring, each DU is equipped with a filter and calibration wheel assembly<sup>10</sup> (Figure 6.6). These assemblies contain various radioactive sources that can be rotated in front of the GPD to provide for monitoring gain, energy resolution, spurious modulation and

IXPE Science Operations Center		
Title: User Guide — Observatory	Document No.: IXPE-SOC-DOC-011	Revision: A
	Effective Date: 2022-07-22	Page: 29 of 69

modulation factor (the sensitivity to polarization for a 100% polarized source) during the mission. The calibration sources will be used in those parts of the orbit when the x-ray source under study is eclipsed by the earth, calibrating one detector at a time.

The calibration sources are all based on  $^{55}\text{Fe}$  isotopes which have a  $K_{\alpha}$  line at 5.9 keV and a  $K_{\beta}$  line at 6.5 keV. Cal source A produces polarized x rays at 3 keV (via a silver target,  $\text{Si L}\alpha = 3 \text{ keV}$ ) and at 5.9 keV, through  $45^{\circ}$  Bragg reflection off a graphite mosaic crystal. Cal sources C and D are unpolarized 5.9 keV and 6.5 keV x rays in a spot ( $\sim 3 \text{ mm}$ ) and flood ( $\sim 15 \times 15 \text{ mm}$ ) configuration respectively. Cal source D utilizes a silicon target in front of the  $^{55}\text{Fe}$  to produce a broad beam at 1.7 keV ( $\text{Si } K_{\alpha}$ ). Expected count rates at the time of launch are given in Table 6.5, averaged over the 3 flight detectors.

In addition to the calibration sources the wheel also contains an open position, a closed position and an attenuator position consisting of a  $75\text{-}\mu\text{m}$ -thick kapton foil coated with 100 nm of aluminum on each side. The first of these is for normal operations, the second for internal background measurements and the third is for observing very bright sources which would otherwise exceed the throughput of the system.

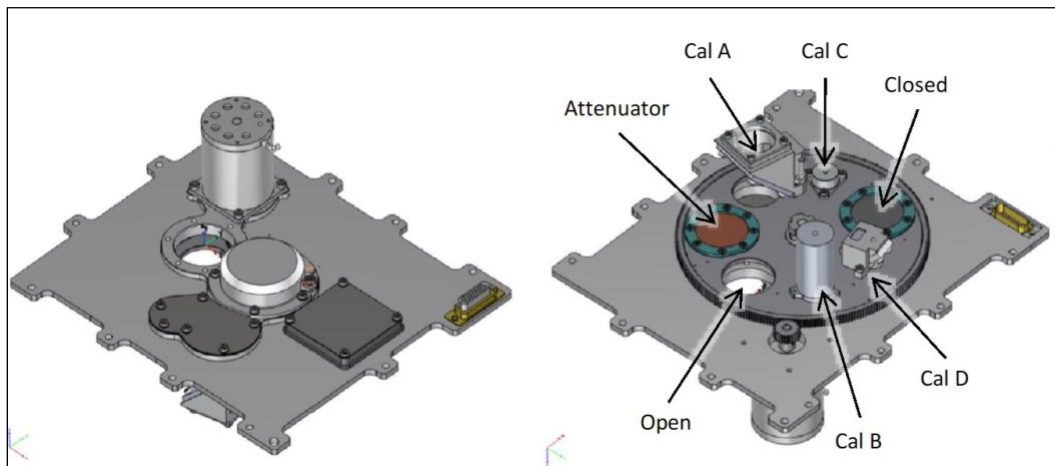


**Figure 6.6:** Filter and calibration wheel assembly (left: top view (+z); right: bottom view (-z))

Cal Source	Count / Sec
A (5.9 keV)	33
A (3.0 keV)	2.5
B (5.9 + 6.5 keV)	62
C (5.9 + 6.5 keV)	119
D (1.7 keV)	78

**Table 6.5:** Expected count rates from on-board sources at launch

### 6.3 Detectors Service Unit (DSU)

The principal task of the DSU is to format the DU data in a way suitable for storage in the spacecraft memory (5 GByte) and S-band downloading. The DSU also controls the filter and calibration wheels, manages the different operational modes of the DUs and supplies the necessary

IXPE Science Operations Center		
Title: User Guide — Observatory	Document No.: IXPE-SOC-DOC-011	Revision: A
	Effective Date: 2022-07-22	Page: 30 of 69

low-voltages. Specifically, the DSU provides the following functions for the operation and autonomy of the IXPE instrument:

- (1) Power supply generation (secondary power to supply the DU's sub-units)
- (2) Telemetry management (data acquisition, formatting, and transmission to the S/C)
- (3) Command management (reception, verification, generation, scheduling, distribution, and execution).
- (4) Time management (synchronization of the three DUs, GPS pulse per-second distribution, and time tagging)
- (5) Filter and calibration wheel management
- (6) Science data management (retrieving, isolated pixels removal, formatting, and transmission to the spacecraft integrated avionics unit)
- (7) Payload mode control
- (8) GPD temperature control
- (9) Fault detection isolation and recovery (FDIR) management

The DSU consists of two boards with cold redundancy and one backplane for internal DSU signal routing. The boards are the single board computer and the power and service board. IXPE uses a centralized solid-state memory bank within the spacecraft for data storage and transmission. The memory onboard the DSU is used only to store the boot software and support the internal operations. The DSU received power from the spacecraft on two (one nominal and one redundant) unregulated power lines on separate connectors. The nominal voltage of the power lines is 28 V. Minimum and maximum values of input power provided by S/C are, respectively, 26 V and 34 V.

## 6.4 Instrument Operation

### 6.4.1 Modes of operation

The instrument modes of operation are managed by the DSU and are selected either via tele-command or by activating autonomously an on-board procedure set by an alarm condition which puts the instrument in a safe mode.

The modes of operation are as follows (see also Figure 6.7):

1. Boot, is a transitional start-up mode that occurs at power on. Boot software, runs from the programmable read-only memory (PROM) in order to perform all checks and initialization of the instrument. In the nominal case, the application software completes the initialization sequence by placing the instrument in standby mode (see below). The boot phase lasts around 60 s.
2. Maintenance. This mode is reserved to support the on-orbit maintenance program.
3. Stand-by. Nominally, at the end of the boot phase, the DSU transitions into stand-by mode to start the instrument monitoring and control. The stand-by mode supports: starting and handling of the thermal regulation; powering on and off the instrument systems; processing of the incoming tele-commands; and the generation of the related outgoing telemetry. Finally, it configures the detector units and the science data processing.

IXPE Science Operations Center		
Title: User Guide — Observatory	Document No.: IXPE-SOC-DOC-011	Revision: A
	Effective Date: 2022-07-22	Page: 31 of 69

4. Observation. From the point of view of the DSU, all instrument calibration and scientific modes are managed into a unique observation mode that is configured while in stand-by mode. The observation mode supports the handling of thermal regulation, the handling of the time-of-day message, the collection of the housekeeping, and the generation of the scientific data.

5. South Atlantic Anomaly (SAA). This mode is used when the satellite crosses the South Atlantic Anomaly which happens once per orbit. In this mode, the high voltage (HV) is ramped down below the voltage necessary for gas multiplication and the science data generation is disabled, while housekeeping data are generated and collected as usual.

6. Safe. This mode is used before switching off the instrument or performing an SW reboot and managing fault detection conditions. This mode preserves DU and HV status (i.e., no HV ramp down or switching off) when entered by telecommand. If entered by a fault condition, the HVs are ramped off, the DUs switched off, and the Filter and Calibration Wheels (FCW) rotation is set to closed as part of the recovery action. In this operation mode, the instrument generates and collects housekeeping only. It is possible to perform a reboot of the application software only during the safe mode.

7. Reboot (transitional mode). At the DSU switch-on, after the boot activities, the application software is loaded into SRAM and executed it checks the position of the FCWs and the status of the detector units and high-voltage boards. If the FCWs are closed and the high voltages are off, the software moves to standby mode. If the FCWs are not closed or if the HVBs are ON, the application software moves the FCWs to the closed position, performs the ramp-off procedure of any high voltages greater than zero, switches off the DUs, and moves the operative mode to safe.

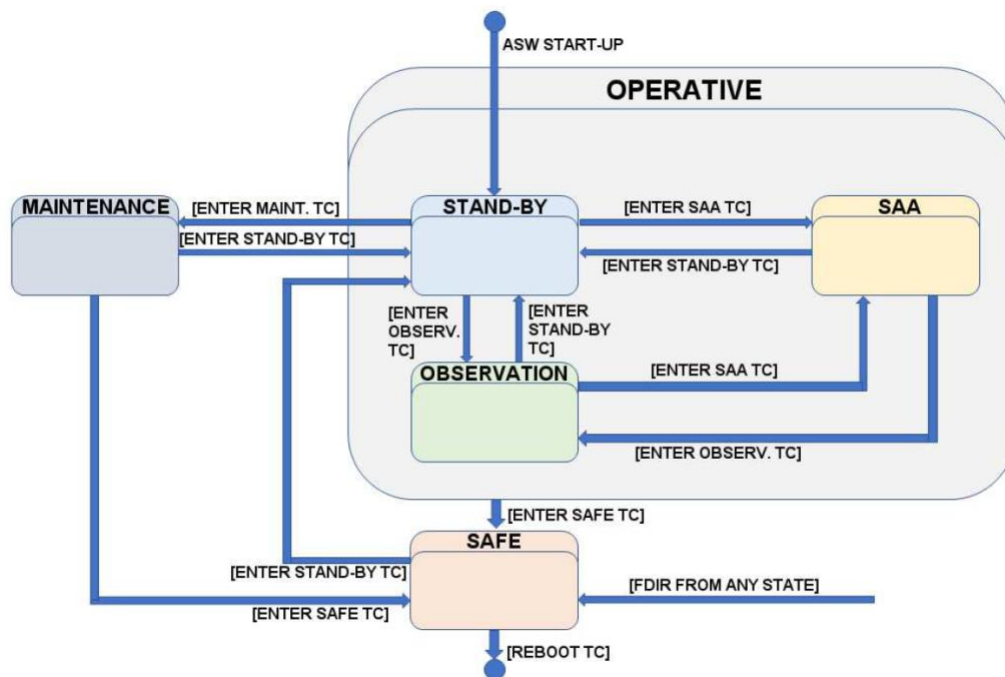


Figure 6.7: IXPE Instrument modes of operation

IXPE Science Operations Center		
Title: User Guide — Observatory	Document No.: IXPE-SOC-DOC-011	Revision: A
	Effective Date: 2022-07-22	Page: 32 of 69

### 6.4.2 Dead time / rate capability

The dead time per event  $Td$  depends on the specifics of the readout sequence and can in general be factored into two different terms one constant and one proportional to the number of pixels  $npix$  in the region of interest:  $Td = d + m npix$ . The two coefficients depend on the particular readout settings of the back-end electronics: roughly speaking,  $m$  is mainly determined by the clock period of the serial readout while  $d$  relates to the timing constraints imposed by the ASIC for a correct readout, and particularly the fixed delay ( $\geq 400\mu s$ ) needed between two successive readouts. Both figures further depend on the number of additional event readouts used for the pedestal subtraction. In the nominal data-taking configuration  $d \sim 750 \mu s$  and  $m \sim 600$  ns per pixel, yielding an average dead time per event slightly in excess of 1 ms for a typical ROI of 500 pixels. For one of the brightest sources planned, the Crab Nebula, this gives about 9% deadtime.

### 6.4.3 Hot pixel masking

Each DU has a specific list of noisy pixels evaluated at various times during GPD acceptance tests, DU AIV/T, DU Calibration and Instrument end-to-end tests. This list is used to mask of the noisy pixels to avoid fake triggers which could impact the data rate. The list can be evaluated and updated on board at any time if new noisy pixels appear. These can be detected on the ground with specific algorithms that analyze nominal acquisitions, both from celestial sources or calibration sources. If a pixel is masked its signal does not contribute to the trigger within its mini-cluster. It is worth noticing that since the trigger is formed by groups of 4 pixels, masking only one or two of the same mini-cluster has a small effect on the trigger efficiency if the threshold is reasonably low.

The GPD is typically operated at an effective trigger threshold of  $\sim 1000$  electrons, which masks off just a handful of pixels (fewer than 1 in 10,000) and gives a noise-trigger rate of  $\ll 1$  c/s. Masking the pixels involves an acquisition of just electronic noise or an acquisition with calibration sources, recording the count rate rate of each pixel, and select those with  $\gg 1$  c/s. A mask is then uploaded with the coordinates of the noisy pixels recorded and checked through housekeeping.

### 6.4.4 Timing

The GPD provides, for each processed event, a trigger output which is used to time tag each event with  $1 \mu s$  resolution and 1-2 us accuracy, based on the pulse-per-second from the GPS and the instrument's 1-MHz Oscillators. The IXPE satellite manages the GPS receiver and provides the signal to the instrument through a dedicated line. The spacecraft also provides the time of day with a frequency of 1 Hz. The TOD also contains information about the validity of the previously provided PPS and the time of the next PPS.

The DSU is equipped with a temperature-compensated 1-MHz crystal oscillator (TCXO) with an accuracy  $< 4$  ppm. The PPS and the 1 MHz clock generated by the 1 MHz local oscillator are provided to each DU.

The onboard time (OBT) management is based on a master OBT implemented in the DSU and 3 local OBTs implemented in the DUs. The master OBT and the locals OBTs are composed of (i) a 29 bit counter for the seconds ( $> 16$  yr of mission lifetime) and (ii) a 20 bit counter for the microseconds ( $1 \mu s$  resolution) and a register for the OBT error (error counter). At boot, the master OBT is initialized by subtracting the start mission date (stored in the DSU MRAM) from the GPS

IXPE Science Operations Center		
Title: User Guide — Observatory	Document No.: IXPE-SOC-DOC-011	Revision: A
	Effective Date: 2022-07-22	Page: 33 of 69

time. During nominal observation, when the GPS is valid, the second counter is incremented upon receiving the PPS and the microsecond counter is incremented by the 1 MHz local oscillator. At the arrival of the PPS, the difference of the microsecond counter with respect to  $10^6$  is stored in the Master OBT error counter and included in the housekeeping data packet. The local OBTs in each DU are updated by the back end electronics in the same way, using the PPS and the DSU (TCXO) clock (see Figure 6.8).

If the previous PPS is not valid, as indicated by the TOD, the PPS provided by the S/C is not used. The DSU synthesizes the PPS for the DUs using the local TCXO. During this operation mode, the OBT error is set equal to zero. The non valid condition information is included in the housekeeping (HK) data. The master OBT remains in free running until the reception of the sequence of TOD reporting that the PPS is again valid. In this case the DSU re-initializes the instrument timing as it would at instrument boot.

The alignment of the local OBT with the master OBT is verified using the housekeeping telemetry (TM). The HK telemetry (TM) compares the values of the local OBTs and the master OBT every second. At the MOC/SOC, these values are monitored and in cases of discrepancy, a pre-arranged action is carried out to get the times back in sync (e.g., time reset by telecommand).

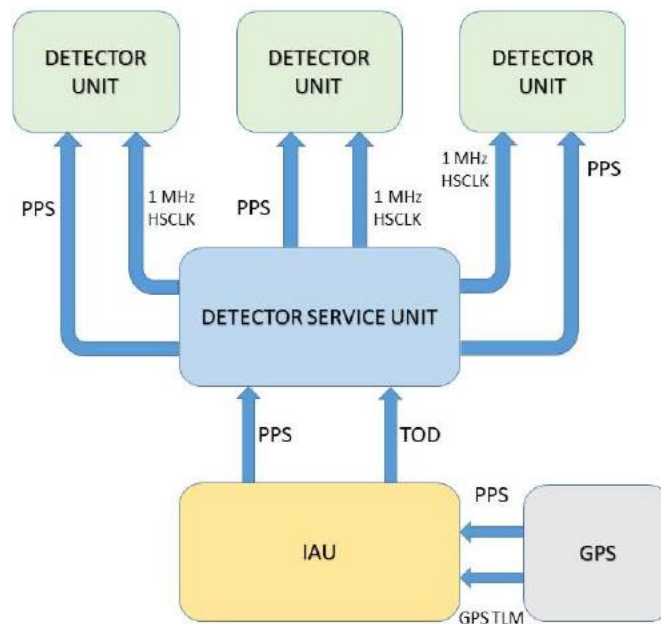


**Figure 6.8:** IXPE Instrument timing architecture

## 6.5 Data Analysis

### 6.5.1 Event reconstruction

Loosely speaking, the word *reconstruction* refers to the processing of raw data that is necessary to extract, on an event-by-event basis, the physical information of interest, i.e., our best estimates for the arrival time, energy and absorption point of the photon, as well as the direction of emission of

IXPE Science Operations Center		
Title: User Guide — Observatory	Document No.: IXPE-SOC-DOC-011	Revision: A
	Effective Date: 2022-07-22	Page: 34 of 69

the photo-electron. Despite the renewed interest in the investigation of novel track reconstruction algorithms for photoelectric x-ray polarimetry<sup>11,12</sup>, including the application of deep learning techniques<sup>13</sup>, our baseline reconstruction strategy at the time of launch, that we shall briefly review here, is essentially the one described in<sup>14</sup>, chosen as the best compromise between effectiveness and robustness against possible systematic effects. We anticipate that we shall deploy an update of the data processing pipeline, based on the work described in<sup>15,16</sup>, as soon as the latter is thoroughly tested on ground calibration data. All the tests that we have performed indicate that this update will allow for a significant enhancement of the IXPE polarization sensitivity.

The very first step of the reconstruction is fixed-threshold zero suppression, where pixels in the region of interest whose pedestal-subtracted signal is below a given value (typically of the order of two noise  $\sigma$ ) are simply masked and ignored in all the subsequent steps. The zero-suppressed data stream is then passed on to a clustering stage, based on the DBSCAN algorithm<sup>17</sup>, grouping together all the contiguous pixels above threshold. The largest cluster is taken as the basic representation of the photo-electron track, that the following steps of the event reconstruction operate on. From the standpoint of the reconstruction, a track is essentially a list of pixels, each fully characterized by a position  $(x_i; y_i)$  on the readout plane and a pulse height  $q_i$ . The sum of the pixel signals over the track represents our best estimate of the event energy.

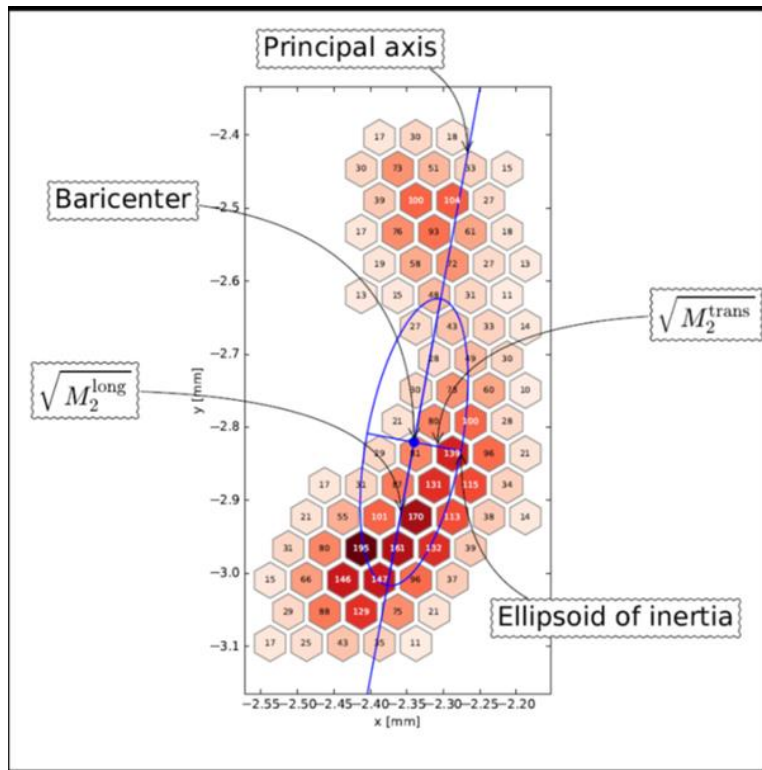


**Figure 6.9:** Illustration of the first-step moments analysis on a real photo-electron track from a 5.9 keV photon. The principal axis of the track, along with the ellipsoid of inertia are overlaid in blue. We note that the relatively larger ionization density corresponding to the Bragg peak at the bottom of the image is our main discriminant in identifying the initial part of the track and seed the second-pass weighted moments analysis that is illustrated in Figure 6.10.

IXPE Science Operations Center		
Title: User Guide — Observatory	Document No.: IXPE-SOC-DOC-011	Revision: A
	Effective Date: 2022-07-22	Page: 35 of 69

After the clustering stage, most of the reconstruction flow deals with calculation of basic track properties, as illustrated in Figure 6.9. A first pass, an un-weighted moments analysis around the track barycenter, provides the principal axis of the track as a whole, as well as the eigenvalues  $M_2^{long}$  and  $M_2^{trans}$  of the tensor of inertia of the two-dimensional charge distribution, which are related to the two semi-axes of the ellipsoid of inertia.

$$a = \sqrt{M_2^{long}}$$

$$b = \sqrt{M_2^{trans}}$$

Since the polarization information is encoded in the emission angle of the photoelectron, and the direction of the latter is progressively randomized by multiple scattering in the gas, the principal axis of the track does not provide, in general, the ultimate polarization sensitivity, especially for high-energy events. To take full advantage of information provided by the detector, we project the charge distribution on its principal axis and calculate the skewness of the resulting one-dimensional probability density function. Due to the relatively higher ionization density in the Bragg peak at the end of the track, this allows identification of the initial part of the track. A second-pass moments analysis, where pixels far away from the start of the track are properly de-weighted, allows in general to achieve more accurate estimates of both the position of the absorption point and the emission angle of the photo-electron, as shown in Figure 6.10.

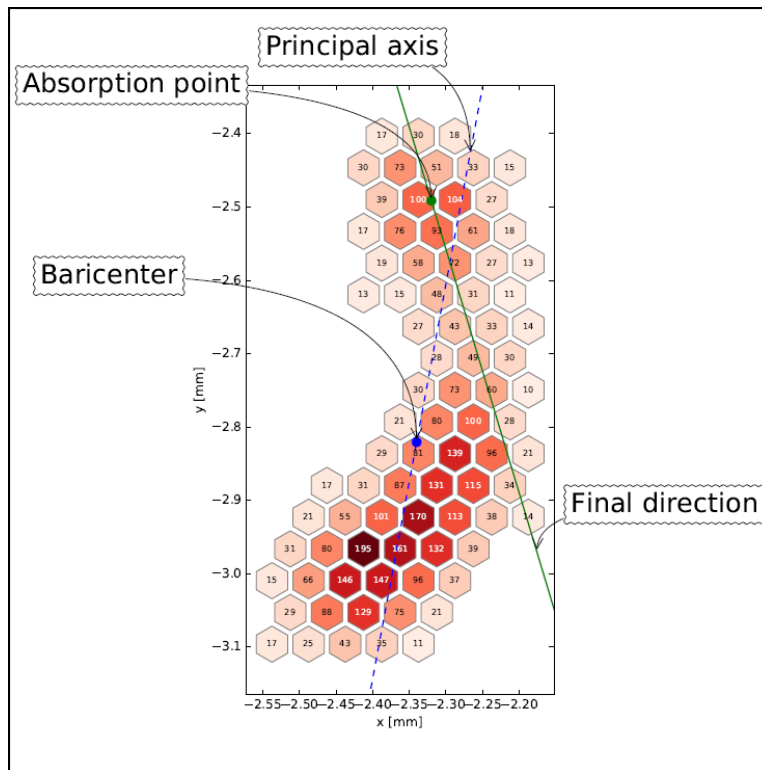


**Figure 6.10:** Illustration of the second-step moments analysis on a real photo-electron track from a 5.9 keV photon. The weighted moments analysis following the identification of the initial part of the track allows for a substantial improvement of both the imaging and polarization capabilities of the detector.

IXPE Science Operations Center		
Title: User Guide — Observatory	Document No.: IXPE-SOC-DOC-011	Revision: A
	Effective Date: 2022-07-22	Page: 36 of 69

## 6.5.2 Calibration and removal of spurious effects

The basic reconstruction strategy outlined in the previous section relies on a number of corrections that will be implemented in the processing pipeline run at the IXPE Science Operations Center (SOC). Although a detailed description of the complex data processing sequence is outside the scope of this paper, we outline the basic steps in the following list:

1. Correction for trigger-induced electronics effects in the readout chip
2. Pixel-by-pixel equalization of the response
3. Bad pixel identification and removal
4. Track reconstruction
5. Correction for temperature-induced gain variations
6. Correction for rate-dependent gain variations induced by charging effects
7. Correction for high-voltage setting and secular pressure variations and calculation of the pulse invariant
8. Subtraction of the spurious modulation in the Stokes parameter space
9. Projections of the absorption point and the Stokes parameters in the sky based upon the aspect solution of the telescope

While most of these steps are quite standard, at least in the basic intent (e.g., the pixel equalization and the projection of the polarization direction in sky coordinates), it is worth giving a succinct overview of two effects that are specific to IXPE: the correction for the rate-dependent gain variations due to a charging effect and the subtraction of the spurious modulation. We emphasize that the standard photon lists distributed through HEASARC will include all these corrections, that will therefore be largely transparent to the end user (although they will have all the software tools and associated calibration data products available for re-running the entire processing chain).

As explained in<sup>18</sup>, when the GPD is irradiated, part of the charge from the avalanche in the multiplication stage can be temporarily deposited onto specific regions of the dielectric substrate, which in turns tends to modify the configuration of the electric field, causing measurable changes in the gain. This rate-dependent effect, typical of many classes of gas detectors, in our case is exacerbated by the fine pitch of the IXPE gas electron multipliers, which makes the ratio between the hole volume and the exposed surface particularly unfavorable. From the standpoint of the scientific performance, the charging manifests itself as a time-dependent gain variation up to ~ 10%, with associated time scales ranging from minutes to days, and an asymptotic value that depends on the energy flux per unit area of the particular source being observed. Proper correction of this effect is important for the measurement of both the absolute source flux and, more importantly, the polarization, because the modulation factor is strongly energy dependent.

The effect is qualitatively similar across different detectors, but each one requires its specific calibration. We developed a complete phenomenological model and measured the corresponding parameters detector by detector as part of the ground calibrations. In flight we shall exploit the spectral and imaging capabilities of the GPD to monitor the energy flux as a function of time and position across the active area during the observation, and integrate the model to correct the gain.

IXPE Science Operations Center		
Title: User Guide — Observatory	Document No.: IXPE-SOC-DOC-011	Revision: A
	Effective Date: 2022-07-22	Page: 37 of 69

Periodic data taking runs with the on-board calibration sources will allow one to anchor the correction to the known energy of the radioactive sources in the filter and calibration wheel and prevent any possible long-term trending in the correction. The reader is referred to<sup>18</sup> for a more complete treatment of the formalism and the details of the modelling and correction.

The second effect that we briefly discuss here is the removal of the low-energy spurious modulation<sup>19,18,20</sup>, a residual asymmetry in the intrinsic azimuthal response of the gas pixel detectors amounting to an average amplitude of  $\sim 1\%$  at 2.7 keV, rapidly decreasing with energy, and varying over spatial scales smaller than the PSF of the IXPE optics, when projected on the detector surface. (The reader is referred to<sup>18</sup> for a more extended discussion of the instrumental origin of this effect.) The correction, which is necessary to achieve the IXPE science goals, takes places entirely in Stokes parameter space. More precisely, given the best estimate of the photo-electron emission angle  $\phi_i$  for a given event, we define the quantities

$$q_i = 2 \sin(2\phi_i)$$

$$u_i = 2 \cos(2\phi_i)$$

The spurious modulation ( $q_s, u_s$ ) has been mapped for each detector unit on a grid of discrete energies as a part of the ground calibrations<sup>21</sup>, and these maps, interpolated in energy, will be used in the SOC processing pipeline to correct the event-by-event Stokes parameters in the cleaned photon lists that will be delivered by the HEASARC

$$q_i \rightarrow \tilde{q}_i = q_i - q_s(E_i, x_i, y_i) \quad (1)$$

$$u_i \rightarrow \tilde{u}_i = u_i - u_s(E_i, x_i, y_i)$$

We emphasize that the effectiveness of this correction relies on the dithering of the observatory, that helps averaging the effect on the detector surface, as mapping it down to the scale of the PSF would have required prohibitively long calibration times.

Although in general the corrected Stokes parameters ( $\tilde{q}_i, \tilde{u}_i$ ), unlike the original ones derived from the reconstructed photo-electron angle, are not properly normalized, i.e.

$$\tilde{q}_i^2 + \tilde{u}_i^2 \neq 4$$

and cannot readily be transformed back into an azimuthal angle, this methods can be demonstrated to provide the correct answer, on average, for any ensemble of events, and it has the definite advantage that the user does not need to calculate any correction that is specific to the desired selection in energy, sky coordinates, or time. A full description of the subtraction method and its statistical properties is given in<sup>20</sup>.

### 6.5.3 Event weighting

Along with relevant Physics observables, the baseline event reconstruction provides a rich set of diagnostic information, encapsulating much of the rich morphology of the track images on the GPD, in a form that can be effectively used in the event-level analysis. The eigenvalues  $M_2^{long}$  and  $M_2^{trans}$  of the tensor of inertia of the charge distribution, specifically, can be combined<sup>22</sup> to provide an elongation normalized parameter:

IXPE Science Operations Center		
Title: User Guide — Observatory	Document No.: IXPE-SOC-DOC-011	Revision: A
	Effective Date: 2022-07-22	Page: 38 of 69

$$\alpha = \frac{M_2^{long} + M_2^{trans}}{M_2^{long} + M_2^{trans}}$$

that can be effectively used to enhance the IXPE polarization sensitivity. (We note explicitly that  $\alpha = 0$  when the ellipsoid of inertia of the track degenerates into a circle and  $\alpha \rightarrow 1$  when the major semi-axis is much longer than the minor one, i.e., the track is very elongated.)

While the fact that, at any given energy, more elongated tracks tend to be better reconstructed does not come as a surprise, we empirically found  $\alpha$  to be a good proxy of the modulation factor for any event, which in turn was demonstrated in<sup>16</sup> to be the optimal weighting for polarimetry data. More specifically we found that, when used as an event-by-event weight, the quantity

$$w_i = \alpha_i^{0.75}$$

allows to improve the IXPE polarization sensitivity (or, more precisely, the broadband minimum detectable polarization between 2 and 8 keV) by 10–15% depending on the source spectrum. Accordingly, this is included by default as one of the columns in the cleaned photon lists, and the IXPE CALDB is equipped with response functions suitable to be used in a weighted spectro-polarimetric analysis.

#### 6.5.4 Detector response and high-level science analysis

While most of the description of the detector response for IXPE is not dissimilar from that of other x-ray instruments (the CALDB, e.g., will include the effective area and the response matrix in the standard OGIP-compliant format), there are aspects related to polarization that are substantially new for the x-ray community that we briefly outline here.

IXPE Science Operations Center		
Title: User Guide — Observatory	Document No.: IXPE-SOC-DOC-011	Revision: A
	Effective Date: 2022-07-22	Page: 39 of 69

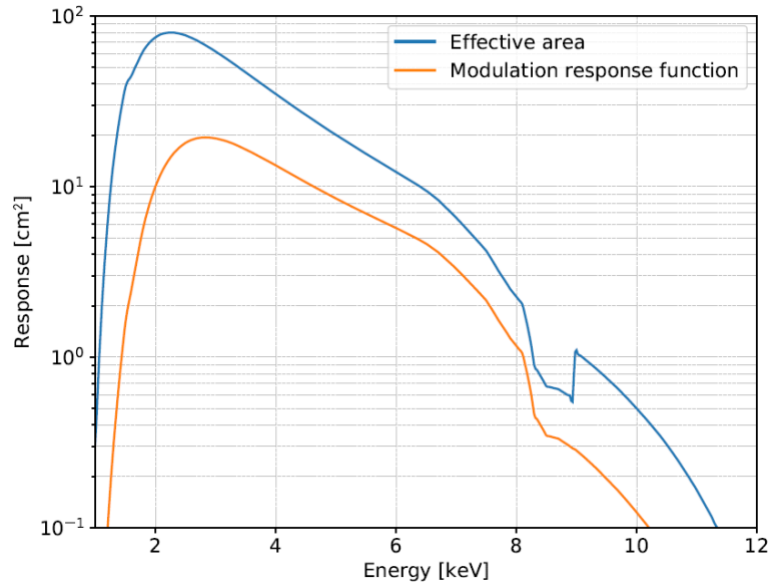


**Figure 6.11:** Pre-launch preliminary estimate of the combined on-axis effective area and modulation response function for the three IXPE telescopes. We emphasize that the three IXPE telescopes will have slightly different response functions and, while the combined figure provides a good proxy of the overall sensitivity of the observatory, any science analysis will require a combined maximum likelihood in which the spectra from each telescope will have the proper response files associated with it.

We define the modulation response function as the product of the effective area  $A_{eff}$  and the modulation factor  $\mu$ , as a function of the (true) photon energy  $E$

$$R(E) = A_{eff}(E) \times \mu(E)$$

Just like the effective area, the modulation response function is expressed in units of  $\text{cm}^2$ , and, therefore, it will be distributed in a FITS format identical to the standard .arf files. For illustrative purposes, Figure 6.11 shows a pre-launch estimate of the combined effective area and modulation response function for the three IXPE telescopes. The peak effective area is of the order of  $\sim 80 \text{ cm}^2$  while, the modulation factor being  $\leq 1$  and increasing with energy, the modulation response function is generally smaller, and peaking at a somewhat higher energy.

The basic spectro-polarimetric analysis for a typical point source is a straightforward generalization of the forward-folding, maximum likelihood technique implemented, e.g., in XSPEC. More specifically, one can create binned spectra for the two Stokes parameters (eqi; eui) defined in Equation (1) in the form of weighted histograms analogous to the standard .pha files, with the modulation response function (as opposed to the effective area) used as the associated ancillary response file. For completeness, the public archive of XSPEC local models includes a number of simple, phenomenological multiplicative models for spectro-polarimetry<sup>1</sup> that can be effectively used for science analysis and as a guide to implement more complex models.

IXPE Science Operations Center		
Title: User Guide — Observatory	Document No.: IXPE-SOC-DOC-011	Revision: A
	Effective Date: 2022-07-22	Page: 40 of 69

## 7 TELESCOPE PERFORMANCE (GROUND CALIBRATION OF SPARE UNITS)

An IXPE telescope, comprising the spare mirror module assembly (MMA4) and the spare detector unit (DU-FM1), was calibrated at the MSFC stray light test facility from 12/8/2020 through 1/19/2021. A comprehensive set of calibration data had already been taken for the individual detector units in Italy and for the individual MMAs at MSFC. The calibration reported here provides data to verify that a telescope response can be derived from an analytical combination of mirror module calibration data and detector unit calibration data. For additional information on the telescope calibration see IXPE-RPT-181, Rev.A. dated 7/12/2021.

### 7.1 Angular Resolution

Prior to making measurements, the DU was centered and a best-focus position<sup>2</sup> was obtained. Angular resolution (half-power diameter) data were collected as the MMA was stepped through the required onaxis and off-axis angles. As rotating the optic about its node does not move the focal image, the detector must also be stepped to appropriate off-axis positions to simulate in-flight performance. Table 7.1 shows the angles covered, and their respective nominal detector positions.

MMA Off-axis angle (arcmin)		Detector Offset (mm)	
Pan	Tip	X	Y
0	0	0	0
0	5.0	0	6.05
0	-5.0	0	-6.05
5.0	0	6.05	0
-5.0	0	-6.05	0
4.95	4.95	5.99	5.99
4.95	-4.95	5.99	-5.99
-4.95	4.95	-5.99	5.99
-4.95	-4.95	-5.99	-5.99
0	3.0	0	3.63
0	-3.0	0	-3.63
3.0	0	3.63	0
-3.0	0	-3.63	0
2.83	2.83	3.42	3.42
2.83	-2.83	3.42	-3.42
-2.83	2.83	-3.42	3.42
-2.83	-2.83	-3.42	-3.42

**Table 7.1:** Off-axis angles and detector positions for telescope HPD measurements

---

<sup>2</sup> Note that MMAs are slightly defocused on the observatory. See section 5.2.4 for discussion and assessment.

IXPE Science Operations Center		
Title: User Guide — Observatory	Document No.: IXPE-SOC-DOC-011	Revision: A
	Effective Date: 2022-07-22	Page: 41 of 69

Data were taken at Mo L (2.3 keV), Ti K (4.6 keV, weighted mean) and Fe K (6.6 keV, weighted mean) using Nb (5  $\mu\text{m}$ ), Ti (77  $\mu\text{m}$ ) and Fe (77  $\mu\text{m}$ ) filters respectively.

The DU data were processed using an energy cut of  $\pm 3 \sigma$  on all measured line energies. The origination points for the photoelectron tracks were taken as the simple charge barycenter for the Mo measurements and as the calculated impact point from the track analysis for the Ti and Fe measurements. For consistency, the half-power diameter was calculated taking a DU region 8 mm in diameter, as this was the size of the silicon drift detector used by MSFC to derive the MMA effective area. This diameter extends out to about 16 times the measured HPD and contains essentially all the focused flux and minimal background (the source rate is 1000 $\times$  the background rate). The resulting HPD (in mm) was divided by the telescope's finite source distance focal length (4.17 m at the 100-m-long Stray Light Test Facility) to give angular resolutions shown in Tables 7.2, 7.3 and 7.4 below.

MMA Off-axis angle (arcmin)		HPD ( $\mu\text{m}$ )	HPD (arcsec)
Pan	Tip		
0	0	448.2	22.2
0	5.0	474.4	23.5
0	-5.0	480.2	23.8
5.0	0	502.8	24.9
-5.0	0	471.8	23.4
4.95	4.95	498.9	24.7
4.95	-4.95	526.3	26.1
-4.95	4.95	480.0	23.8
-4.95	-4.95	488.2	24.2
0	3.0	465.9	23.1
0	-3.0	465.9	23.1
3.0	0	478.2	23.7
-3.0	0	462.7	22.9
2.83	2.83	483.8	24.0
2.83	-2.83	485.1	24.0
-2.83	2.83	465.4	23.0
-2.83	-2.83	472.4	23.4

**Table 7.2:** Measured telescope HPD as a function of off-axis angle at 2.3 keV. HPD 1- $\sigma$  uncertainties are  $\sim \pm 0.5\%$ .

MMA Off-axis angle(arcmin)		HPD ( $\mu\text{m}$ )	HPD (arcsec)
Pan	Tip		
0	0	481.6	23.8
0	5.0	516.1	25.6
0	-5.0	515.3	25.5
5.0	0	529.0	26.2
-5.0	0	513.9	25.4
4.95	4.95	532.5	26.4
4.95	-4.95	563.0	27.9
-4.95	4.95	522.1	25.9
-4.95	-4.95	533.6	26.4
0	3.0	505.0	25.0
0	-3.0	505.0	25.0
3.0	0	519.1	25.7
-3.0	0	503.1	24.9
2.83	2.83	520.5	25.8
2.83	-2.83	525.0	26.0
-2.83	2.83	500.7	24.8
-2.83	-2.83	513.6	25.4

**Table 7.3:** Measured telescope HPD as a function of off-axis angle at  $\sim 4.6$  keV. HPD  $1\text{-}\sigma$  uncertainties are  $\pm 1\%$ .

MMA Off-axis angle (arcmin)		HPD ( $\mu\text{m}$ )	HPD (arcsec)
Pan	Tip		
0	0	485.7	24.1
0	5.0	530.7	26.3
0	-5.0	564.3	27.9
5.0	0	549.3	27.2
-5.0	0	537.9	26.6
4.95	4.95	542.4	26.9
4.95	-4.95	579.8	28.7
-4.95	4.95	548.5	27.2
-4.95	-4.95	552.4	27.4
0	3.0	527.6	26.1
0	-3.0	536.7	26.6
3.0	0	538.6	26.7
-3.0	0	526.4	26.1
2.83	2.83	542.1	26.8
2.83	-2.83	555.8	27.5
-2.83	2.83	529.8	26.2
-2.83	-2.83	529.2	26.2

**Table 7.4:** Measured telescope HPD as a function of off-axis angle at  $\sim 6.6$  keV. HPD  $1\text{-}\sigma$  uncertainties are  $\pm 1\%$ .

IXPE Science Operations Center		
Title: User Guide — Observatory	Document No.: IXPE-SOC-DOC-011	Revision: A
	Effective Date: 2022-07-22	Page: 43 of 69

### 7.1.1 Comparison of Measured to Predicted Telescope Half Power Diameter

The half-power diameter of each MMA was measured using a CCD camera at the focus of the optic, with filtered x-ray sources producing lines at nominally 2.3 keV (MoL), 4.5 keV (TiK) and 6.4 keV (FeK) along with some continuum emission. The detector region used for this measurement was chosen to be the same as that used for the effective area—i.e., an 8-mm-diameter circle, which is approximately 16 times the MMA HPD. Flat fields, taken immediately before and after measurements, were used to subtract offsets and noise contributions in individual pixels. The diameter containing half the flux within the measurement region was then determined and converted to an angle using the measured image distance ( $\sim 4.17$  m) for the 100-m object distance at the SLTF.

For the telescope, the HPD was measured at the same energies as was the MMA, using the same 8-mm-diameter circular region on the DU. As with the MMA, the diameter containing half the flux within this region was calculated and converted to an angle, again using the same measured focal distance (image distance).

It is expected that the telescope and MMA HPDs will differ slightly. This is because the DU adds additional blurring to the image due to its finite spatial resolution (limited by the ability to determine the beginning of a track) and by the finite depth of the detector (10 mm), which adds additional defocusing of the image due to gas transparency and the cone angle of x rays focused by the mirror assembly. However, these two components are small compared to the native MMA resolution.

The detector spatial resolution was measured during calibration in Italy<sup>1</sup>. An additional factor has been added to these reported spatial resolutions to account for a slight (measured) misalignment of the DU with respect to the x-ray axis during the telescope calibration.

Defocusing effects, due to finite detector gas depth, were calculated via Monte-Carlo simulations. As a check, results were also obtained by taking a series of CCD images over a  $\pm 5$ -mm region centered on the optimum focal distance, to span the region covered by the thickness of the detector gas cell. Summing these CCD images effectively blurs the image similarly to that due to the gas depth in the DU. These measurements agreed very well with the Monte-Carlo simulations (within a fraction of an arcsecond).

Table 7.5 shows the results of the on-axis HPD comparison. MMA HPD represents the angular resolution of the MMA measured with the CCD camera. Detector spatial resolution and defocusing effects, converted to HPD in arcsec, are summed in quadrature with the native MMA resolution to give the predicted telescope angular resolution. The final column shows the measured telescope HPD obtained during telescope calibration. Estimated uncertainties are  $\sim 2\%$  ( $1\sigma$ ) for the predicted HPD measurements and  $\sim 0.5$ - $1\%$  for the measured value as given in each table caption. As can be seen from the table, the predicted and measured telescope HPDs are in reasonable agreement given measurement uncertainties.

IXPE Science Operations Center		
Title: User Guide — Observatory	Document No.: IXPE-SOC-DOC-011	Revision: A
	Effective Date: 2022-07-22	Page: 44 of 69

X-ray Tube (Line)	MMA HPD (arcsec)	Detector Spatial Resolution (arcsec)	Detector Defocusing Effects (arcsec)	Predicted Telescope HPD (arcsec)	Measured Telescope HPD (arcsec)
2.3 keV	20.0	5.6	6.0	21.6	22.2
4.6 keV	20.8	6.3	7.0	22.8	23.8
6.6 keV	20.1	7.4	7.2	22.6	24.1

**Table 7.5:** Comparison of predicted and measured on-axis telescope angular resolution

The same process outlined above was repeated, at each energy, for all off-axis angles. These data are shown in Tables 7.6, 7.7, and 7.8, below.

MMA Off-axis angle (arcmin)		Predicted Telescope HPD (arcsec)	Measured Telescope HPD (arcsec)
Pan	Tip		
0	0	21.6	22.2
0	5.0	23.1	23.5
0	-5.0	23.0	23.8
5.0	0	23.0	24.9
-5.0	0	23.1	23.4
4.95	4.95	23.9	24.7
4.95	-4.95	24.6	26.1
-4.95	4.95	24.9	23.8
-4.95	-4.95	24.6	24.2
0	3.0	22.4	23.1
0	-3.0	22.4	23.1
3.0	0	22.7	23.7
-3.0	0	22.5	22.9
2.83	2.83	22.7	24.0
2.83	-2.83	23.1	24.0
-2.83	2.83	22.7	23.0
-2.83	-2.83	22.9	23.4

**Table 7.6:** Comparison of predicted and measured telescope angular resolution at 2.3 keV. HPD 1- $\sigma$  uncertainties are  $\sim \pm 2\%$  for predicted values and  $\pm 0.5\%$  for measured values.

IXPE Science Operations Center		
Title: User Guide — Observatory	Document No.: IXPE-SOC-DOC-011	Revision: A
	Effective Date: 2022-07-22	Page: 45 of 69

MMA Off-axis angle(arcmin)		Predicted Telescope	Measured Telescope
Pan	Tip	HPD (arcsec)	HPD (arcsec)
0	0	22.8	23.8
0	5.0	24.6	25.6
0	-5.0	24.9	25.5
5.0	0	24.3	26.2
-5.0	0	24.7	25.4
4.95	4.95	25.4	26.4
4.95	-4.95	26.3	27.9
-4.95	4.95	26.1	25.9
-4.95	-4.95	26.1	26.4
0	3.0	23.6	25.0
0	-3.0	23.6	25.0
3.0	0	23.7	25.7
-3.0	0	23.9	24.9
2.83	2.83	24.1	25.8
2.83	-2.83	24.1	26.0
-2.83	2.83	24.0	24.8
-2.83	-2.83	24.3	25.4

**Table 7.7:** Comparison of predicted and measured telescope angular resolution at 4.6 keV. HPD 1- $\sigma$  uncertainties are  $\sim \pm 2\%$  for predicted values and  $\pm 1\%$  for measured values.

MMA Off-axis angle (arcmin)		Predicted Telescope	Measured Telescope
Pan	Tip	HPD (arcsec)	HPD (arcsec)
0	0	22.6	24.1
0	5.0	24.5	26.3
0	-5.0	25.2	27.9
5.0	0	24.5	27.2
-5.0	0	25.1	26.6
4.95	4.95	25.1	26.9
4.95	-4.95	25.9	28.7
-4.95	4.95	26.1	27.2
-4.95	-4.95	25.9	27.4
0	3.0	23.6	26.1
0	-3.0	23.9	26.6
3.0	0	23.8	26.7
-3.0	0	24.1	26.1
2.83	2.83	23.8	26.8
2.83	-2.83	24.5	27.5
-2.83	2.83	24.2	26.2
-2.83	-2.83	24.4	26.2

**Table 7.8:** Comparison of predicted and measured telescope angular resolution at 6.6 keV. HPD 1- $\sigma$  uncertainties are  $\sim \pm 2\%$  for predicted values and  $\pm 1\%$  for measured values.

IXPE Science Operations Center		
Title: User Guide — Observatory	Document No.: IXPE-SOC-DOC-011	Revision: A
	Effective Date: 2022-07-22	Page: 46 of 69

The tables show that the predicted and measured telescope angular resolutions are in reasonable agreement. At each energy, taking the dataset as a whole, there is an offset (measured minus predicted) in resolution plus a statistical fluctuation around that offset. For all energies, the statistical fluctuations are around 2-3% ( $1-\sigma$ ), consistent with the estimated measurement uncertainties. The offset in HPD values, in which predicted values are slightly smaller than measured values, is approximately 3% for 2.3 keV, 5% for 4.6 keV, and 9% for 6.6 keV. It is possible that these slight differences are due to an underestimate of the DU misalignment and/or an underestimate of the projection effects due to the mirror cone angle, each of which gives energy-dependent effects, which are being investigated further. It should be noted that, despite these small differences, the on-axis measured telescope angular resolution is still well within the requirement (28 arcsec HPD) and, of course, will be checked on-orbit through observations of point sources.

## 7.2 Effective Area

Prior to making measurements, the DU was centered and a best-focus position was obtained as per IXPE-CAL-163, Rev B. Angular resolution (half-power diameter) and effective area data were collected at the same time as the MMA was stepped through the on axis position and a series of off-axis angles. As rotating the optic about its node does not move the focal image the detector must also be stepped to appropriate off-axis positions to simulate in-flight performance. Table 7.9 shows the angles covered, and their respective nominal detector positions. These angles align with a subset of those used in MMA calibrations, allowing direct comparisons.

MMA Off-axis angle (arcmin)		Detector Offset (mm)	
Pan	Tip	X	Y
0	0	0	0
0	5.0	0	6.05
0	-5.0	0	-6.05
5.0	0	6.05	0
-5.0	0	-6.05	0
4.95	4.95	5.99	5.99
4.95	-4.95	5.99	-5.99
-4.95	4.95	-5.99	5.99
-4.95	-4.95	-5.99	-5.99
0	3.0	0	3.63
0	-3.0	0	-3.63
3.0	0	3.63	0
-3.0	0	-3.63	0
2.83	2.83	3.42	3.42
2.83	-2.83	3.42	-3.42
-2.83	2.83	-3.42	3.42
-2.83	-2.83	-3.42	-3.42

**Table 7.9:** Off-axis angles and detector positions for telescope effective area measurements

Data were taken with Mo L, Ti K, and Fe K characteristic x rays. To suppress continuum emission each source was filtered using Nb (5  $\mu\text{m}$ ), Ti (77  $\mu\text{m}$ ) and Fe (77  $\mu\text{m}$ ) respectively. A monitor

IXPE Science Operations Center		
Title: User Guide — Observatory	Document No.: IXPE-SOC-DOC-011	Revision: A
	Effective Date: 2022-07-22	Page: 47 of 69

counter, positioned at the MMA, was used to derive the incident flux. This device, an AMPTEK fast Silicon Drift Detector, (SDD) has known collecting area and quantum efficiency. For each energy and angle, a minimum of 1000 counts were collected in the monitor counter to give the desired effective-area accuracy (see Appendix A). As the energy resolution of the DU is about 17% FWHM at 6.4 keV, it cannot resolve the  $K_{\alpha}$  from the  $K_{\beta}$  lines for either Ti or Fe, or the different L lines from molybdenum; therefore, a weighted mean energy was used for these measurements. The data from the monitor SDD, which has high spectral resolution, is the sum all the K lines for each source. The L lines from molybdenum are not resolved by the SDD. The effective weighted energies for the three x-ray sources, correcting for SDD efficiency, are: 2.3 keV for Mo L, 4.6 keV for Ti K and 6.6 keV for Fe K.

Data were processed using a standard moments analysis. As the gas detector has limited energy resolution and has tailing (lower energy events present due to incomplete charge collection), the acceptance band of the DU was opened to  $+3\sigma$  above the peak energy and includes everything below the peak. Similarly, the acceptance band of the SDD detector was opened to include all  $K_{\alpha}$  and  $K_{\beta}$  lines plus any escape peaks or tailing present in the data. DU data were corrected for deadtime, as described in the DU calibration report<sup>3</sup>, and the resulting count rate is divided by the rate in the SDD flux monitor (the same one used for MMA calibration), and multiplied by the flux-monitor area. Finally, the resulting effective areas were scaled to those for infinite source distance, using energy and off-axis-angle dependent correction factors given in Appendix B.

The resulting data are shown below for each energy (see Tables 7.10, 7.11, 7.12). Uncertainties for each measurement (statistical plus uncertainties in detector response and geometry) are given in the table caption.

---

<sup>3</sup> I2C-IAPS-ISE-REP-027, issue i03, 26 October, 2020.

IXPE Science Operations Center		
Title: User Guide — Observatory	Document No.: IXPE-SOC-DOC-011	Revision: A
	Effective Date: 2022-07-22	Page: 48 of 69

MMA Off-axis angle (arcmin)		Effective Area (cm <sup>2</sup> )
Pan	Tip	
0	0	25.4
0	5.0	18.9
0	-5.0	17.8
5.0	0	18.1
-5.0	0	19.0
4.95	4.95	17.0
4.95	-4.95	14.6
-4.95	4.95	15.7
-4.95	-4.95	15.4
0	3.0	21.3
0	-3.0	20.9
3.0	0	19.9
-3.0	0	22.3
2.83	2.83	20.1
2.83	-2.83	19.2
-2.83	2.83	19.2
-2.83	-2.83	19.7

**Table 7.10:** Measured telescope effective area as a function of off-axis angle at ~ 2.3 keV. Effective area 1- $\sigma$  uncertainties are  $\sim \pm 5\%$

MMA Off-axis angle (arcmin)		Effective Area (cm <sup>2</sup> )
Pan	Tip	
0	0	7.4
0	5.0	5.6
0	-5.0	5.5
5.0	0	5.6
-5.0	0	5.6
4.95	4.95	4.7
4.95	-4.95	4.7
-4.95	4.95	4.5
-4.95	-4.95	4.5
0	3.0	6.5
0	-3.0	6.3
3.0	0	6.7
-3.0	0	6.7
2.83	2.83	5.9
2.83	-2.83	6.2
-2.83	2.83	6.0
-2.83	-2.83	5.9

**Table 7.11:** Measured telescope effective area as a function of off-axis angle at ~ 4.6 keV. Effective area 1- $\sigma$  uncertainties are  $\sim \pm 4\%$

IXPE Science Operations Center		
Title: User Guide — Observatory	Document No.: IXPE-SOC-DOC-011	Revision: A
	Effective Date: 2022-07-22	Page: 49 of 69

MMA Off-axis angle (arcmin)		Effective Area (cm <sup>2</sup> )
Pan	Tip	
0	0	2.81
0	5.0	1.70
0	-5.0	1.73
5.0	0	1.75
-5.0	0	1.75
4.95	4.95	1.36
4.95	-4.95	1.31
-4.95	4.95	1.30
-4.95	-4.95	1.35
0	3.0	2.27
0	-3.0	2.25
3.0	0	2.28
-3.0	0	2.23
2.83	2.83	1.97
2.83	-2.83	1.97
-2.83	2.83	1.97
-2.83	-2.83	1.98

**Table 7.12:** Measured telescope effective area as a function of off-axis angle at ~ 6.6 keV. Effective area 1- $\sigma$  uncertainties are  $\sim \pm 2\%$

## 7.2.1 Comparison of Measured to Predicted Telescope Effective Area

The on-axis effective area for the MMA alone was measured during MMA calibration using a pair of identical, fast silicon drift detectors (SDDs), one (near the MMA entrance aperture) monitoring the input flux and the other at the mirror focus. The ratio of the two count rates, adjusted for minor response differences measured during cross calibration, multiplied by the monitor’s active area gives the effective area of the optic as a function of energy. A correction was made for finite-source-distance effects (at the 100-m stray light facility), using data in Appendix B, to give effective areas for on-orbit observations.

To derive a predicted telescope on-axis effective area from separate MMA and DU calibrations, the MMA effective area (corrected to infinite source distance) must be combined with the DU quantum efficiency (QE) during the telescope calibration at MSFC. This requires adjusting the efficiency measured during the DU calibration<sup>4</sup> at IAPS, to correct for a pressure drop between that date and the calibration date at MSFC, using models based on measurements and developed in Italy<sup>5</sup>. It is also very important that the appropriate weighted mean source energy is used when deriving the appropriate DU quantum efficiency as the QE changes with energy.

The results of this comparison between the predicted on-axis telescope effective area and the measured effective area, are shown in Table 7.13 at 3 energies with both data sets corrected to

<sup>4</sup> I2C-IAPS-ISE-REP-027, issue i03, 26 October, 2020.

<sup>5</sup> GPD Workbook, Release 0.9.2, 8 October, 2020.

IXPE Science Operations Center		
Title: User Guide — Observatory	Document No.: IXPE-SOC-DOC-011	Revision: A
	Effective Date: 2022-07-22	Page: 50 of 69

infinite source distance. Statistical and systematic errors are approximately 3% for the predicted effective area ( $1\sigma$ ) and 5%, 4% and 2% respectively ( $1\sigma$ ) for the measured effective areas at 2.3 keV, 4.6 keV and 6.6 keV respectively. Predicted and measured telescope effective areas are within statistical errors for these on-axis measurements, as expected.

Source	Mean Energy $K_{\alpha} + K_{\beta}$ (keV)	Measured MMA Effective Area ( $\text{cm}^2$ )	DU quantum efficiency	Predicted Telescope Effective Area ( $\text{cm}^2$ )	Measured Telescope Effective Area ( $\text{cm}^2$ )
Mo	2.30	167.7	0.155	26.02	25.38
Ti	4.63	196.3	0.038	7.56	7.37
Fe	6.58	176.3	0.015	2.68	2.81

**Table 7.13:** Comparison of predicted and measured telescope effective area on axis

The same process was repeated, at each energy, for all off-axis angles in Table 1. For these, MMA effective areas were measured at a subset of angles using the SDDs (17 angles at 2.3 keV and 5 angles at 4.6 keV and 6.6 keV), then interpolated using CCD data taken at every angle. The resulting effective area data are shown in Tables 7.14, 7.15, 7.16, below.

MMA Off-axis angle (arcmin)		Predicted Telescope Effective Area ( $\text{cm}^2$ )	Measured Telescope Effective Area ( $\text{cm}^2$ )
Pan	Tip		
0	0	26.0	25.4
0	5.0	19.9	18.9
0	-5.0	19.9	17.8
5.0	0	19.8	18.1
-5.0	0	19.8	19.0
4.95	4.95	17.3	17.0
4.95	-4.95	17.2	14.6
-4.95	4.95	17.2	15.7
-4.95	-4.95	17.3	15.4
0	3.0	22.9	21.3
0	-3.0	22.9	20.9
3	0	22.8	19.9
-3	0	22.8	22.3
2.83	2.83	21.3	20.1
2.83	-2.83	21.3	19.2
-2.83	2.83	21.3	19.2
-2.83	-2.83	21.3	19.7

**Table 7.14:** Comparison of predicted and measured telescope effective area at  $\sim 2.3$  keV. Effective area  $1\text{-}\sigma$  uncertainties are  $\sim \pm 3\%$  for predicted values and  $\pm 5\%$  for measured values.

IXPE Science Operations Center		
Title: User Guide — Observatory	Document No.: IXPE-SOC-DOC-011	Revision: A
	Effective Date: 2022-07-22	Page: 51 of 69

MMA Off-axis angle (arcmin)		Predicted Telescope Effective Area (cm <sup>2</sup> )	Measured Telescope Effective Area (cm <sup>2</sup> )
Pan	Tip		
0	0	7.6	7.4
0	5.0	5.8	5.6
0	-5.0	5.8	5.5
5.0	0	5.8	5.6
-5.0	0	5.8	5.6
4.95	4.95	5.0	4.7
4.95	-4.95	4.9	4.7
-4.95	4.95	4.9	4.5
-4.95	-4.95	5.0	4.5
0	3.0	6.6	6.5
0	-3.0	6.6	6.3
3.0	0	6.6	6.7
-3.0	0	6.6	6.7
2.83	2.83	6.2	5.9
2.83	-2.83	6.2	6.2
-2.83	2.83	6.2	6.0
-2.83	-2.83	6.2	5.9

**Table 7.15:** Comparison of predicted and measured telescope effective area at ~ 4.6 keV. Effective area 1- $\sigma$  uncertainties are  $\sim \pm 3\%$  for predicted values and  $\pm 4\%$  for measured values.

MMA Off-axis angle (arcmin)		Predicted Telescope Effective Area (cm <sup>2</sup> )	Measured Telescope Effective Area (cm <sup>2</sup> )
Pan	Tip		
0	0	2.68	2.81
0	5.0	1.70	1.70
0	-5.0	1.70	1.73
5.0	0	1.76	1.75
-5.0	0	1.76	1.75
4.95	4.95	1.38	1.36
4.95	-4.95	1.34	1.31
-4.95	4.95	1.34	1.30
-4.95	-4.95	1.38	1.35
0	3.0	2.15	2.27
0	-3.0	2.15	2.25
3.0	0	2.18	2.28
-3.0	0	2.18	2.23
2.83	2.83	1.92	1.97
2.83	-2.83	1.91	1.97
-2.83	2.83	1.91	1.97
-2.83	-2.83	1.92	1.98

**Table 7.16:** Comparison of predicted and measured telescope effective area at ~ 6.6 keV. Effective area 1- $\sigma$  uncertainties are  $\sim \pm 3\%$  for predicted values and  $\pm 2\%$  for measured values.

IXPE Science Operations Center		
Title: User Guide — Observatory	Document No.: IXPE-SOC-DOC-011	Revision: A
	Effective Date: 2022-07-22	Page: 52 of 69

There is reasonable agreement between predicted and measured off-axis effective areas for all energies tested. The 1- $\sigma$  difference between predicted and measured data sets is 4.5% for 2.3 keV, 3.2% for 4.6 keV, and 2.7% for 6.6 keV, consistent with the statistical uncertainties.

## 7.3 Polarization Response

### 7.3.1 Modulation Factor

The measurement of the telescope modulation factor starts with characterization of the width of the polarized beam for each source. This is because the width of the polarized beam in the dispersion direction is significantly less than the width of the MMA, thus the beam must be stepped through multiple positions to ensure uniform coverage of the optic. The beam characterization is performed, for each polarized source, by driving the MMA to its out-of-focus position (+ 50 mm from true focus) and acquiring an image on the focal plane CCD detector. Analysis of this ring image shows the extent of coverage by the beam and allows calculation of the number of discrete steps (achieved by small rotations on the crystal) needed to give uniform MMA coverage. These images at discrete steps are then summed and the resulting ring image analyzed for uniformity. When acceptable, these parameters are recorded for use when making the modulation factor measurement. This process is repeated for all sources used.

Telescope modulation factors were measured for three source + crystal combinations (see Table 7.17), with source energies and crystal lattice spacings chosen to achieve Bragg angles close to 45°. Consequently, the resulting x-ray beams are nearly totally (linearly) polarized.

X-ray Tube (Line)	Crystal	Energy	Polarization
Rhodium (L)	Germanium (111)	2.7 keV	> 99% at ~45 deg
Titanium (K)	Silicon (220)	4.5 keV	> 99% at ~ 45 deg
Iron (K)	aSilicon (400)	6.4 keV	> 99% at ~ 45 deg

**Table 7.17:** X-ray source + crystal combination for modulation factor measurements

For all measurements of modulation factors, dithering of the MMA was used to simulate the dithering that will be used on orbit. This dithering also approximately aligns with that used for detector calibrations in Italy. Two dithering values were used: 1.78-mm radius and 3.57-mm radius, implemented by lateral motions of the MMA-supporting hexapod. The actual dithering pattern was a Lissajous-type figure, designed to provide near uniform coverage of the dither area.

Source	Dither Radius (mm)	Counts Accrued
Rh (L)	1.78	1.2x10 <sup>6</sup>
Ti (K)	1.78	2.9x10 <sup>5</sup>
Fe (K)	1.78	1.9x10 <sup>5</sup>
Rh (L)	3.57	1.6x10 <sup>6</sup>
Ti (K)	3.57	7.1x10 <sup>5</sup>
Fe (K)	3.57	5.8x10 <sup>5</sup>

**Table 7.18:** Modulation factor measurement dither and count parameters

IXPE Science Operations Center		
Title: User Guide — Observatory	Document No.: IXPE-SOC-DOC-011	Revision: A
	Effective Date: 2022-07-22	Page: 53 of 69

Spurious modulation, measured for each energy during calibration of this detector<sup>6</sup>, was first removed. Then the DU data were processed using a standard moments analysis with a 20% cut on tracks, based on track ovality, and an energy cut of  $\pm 3\text{-}\sigma$  around all line energies. The measured modulation factors for the telescope are then compared to those measured for the DU alone during detector calibration by IAPS in Italy. The results are shown in Table 7.19, together with the  $1\text{-}\sigma$  measurement errors.

Source (Energy)	Dither Radius (mm)	Telescope Modulation Factor DU-FM1 + MMA4	Detector Modulation Factor DU-FM1 @ IAPS
Rh L (2.7 keV)	1.78	29.69 $\pm$ 0.20 %	29.87 $\pm$ 0.12 %
Ti K (4.5 keV)	1.78	45.43 $\pm$ 0.33 %	46.04 $\pm$ 0.14 %
Fe K (6.4 keV)	1.78	57.08 $\pm$ 0.42 %	56.59 $\pm$ 0.09 %
Rh L (2.7 keV)	3.57	29.77 $\pm$ 0.13 %	29.87 $\pm$ 0.13 %
Ti K (4.5 keV)	3.57	46.18 $\pm$ 0.21 %	46.04 $\pm$ 0.14 %
Fe K (6.4 keV)	3.57	56.26 $\pm$ 0.23 %	56.59 $\pm$ 0.09 %

**Table 7.19:** Measured telescope and DU modulation factors

An additional set of data was taken at the Stray Light Test Facility, moving the detector unit so that it viewed the polarized source directly, rather than through the MMA. Because the DU is rate limited to  $\sim 150$  c/s it was necessary to electronically mask the DU to accept only events within a 3-mm-radius circle to approximate the dither area with the MMA. In this way the full 150 c/s could be applied to the central region and the desired number of counts could be obtained in a reasonable timescale. These results are shown in Table 7.20.

Source / Energy	Modulation Factor DU-FM1 at MSFC	Modulation Factor DU-FM1 + MMA4	Modulation Factor DU-FM1 @ IAPS
Rh L (2.7 keV)	29.78 $\pm$ 0.17 %	29.77 $\pm$ 0.13 %	29.87 $\pm$ 0.12 %

**Table 7.20:** Measurements of modulation factors for DU-FM1 at MSFC, without and with optic, and in Italy.

Table 7.19 and Table 7.20 show that modulation factors measured with the telescope are statistically identical (within  $1\text{-}\sigma$ ) to those measured with the DU alone. This shows that for the modulation factor the telescope response can be derived from the DU calibration data alone, and that there are no MMA-induced effects.

### 7.3.2 Spurious Modulation

This measurement utilizes low-flux non-polarized x-ray sources to evaluate low-level modulation inherent in the response of the detector.

As x-ray sources can have a small degree of residual polarization, due to the way the x rays are generated, this must be measured and removed from the data. This is accomplished, for each x-ray source, by splitting the measurement in two and rotating the x-ray head by 90 degrees for the

<sup>6</sup> I2C-IAPS-ISE-REP-027, issue i03, 26 October, 2020.

IXPE Science Operations Center		
Title: User Guide — Observatory	Document No.: IXPE-SOC-DOC-011	Revision: A
	Effective Date: 2022-07-22	Page: 54 of 69

second half of the accumulation. Adding together the two halves then cancels out the effects of the source.

As with the modulation factor measurements, the optic was dithered with a radius of 3.57 mm. However, for the aluminum source the hexapod dither had become unreliable (a lubrication issue) and so the image was spread by simply defocusing the optic by 50 mm to give a suitably sized focal region.

Source (Energy)	Dither Radius (mm)	Counts Accrued
Mo L (2.3 keV)	3.57	3.3x10 <sup>6</sup>
Ti K (4.6 keV)	3.57	3.2x10 <sup>6</sup>
Fe K (6.6 keV)	3.57	* 2.6x10 <sup>6</sup>
Al K (1.5 keV)	Not dithered, but defocused	3.1x10 <sup>6</sup>

**Table 7.21:** Spurious modulation measurement dither and count parameters

Data were processed without applying any track cuts. Table 7.22 shows the spurious modulation results for the first three energies with the source modulation removed. Both the Stokes parameters (q and u) and the modulation and angle (in radians) are given along with their respective 1-  $\sigma$  errors.

Source (Energy)	Q (%)	Q-error (%)	U (%)	U-error (%)	Mod (%)	Mod-error (%)	Phi (rad)	Phi-error (rad)
Mo L (2.3 keV)	-0.264	0.085	0.265	0.085	0.373	0.084	1.18	0.11
Ti K (4.6 keV)	0.017	0.097	0.054	0.097	0.056	0.097	0.63	0.87
Fe K (6.6 keV)	0.19	0.11	-0.14	0.11	0.24	0.11	-0.33	0.23

**Table 7.22:** Spurious telescope modulation measurement at 3 energies after source modulation removal.

For the aluminum source, data from the defocused ring image (no dithering) were analyzed within a 1.5-mm radius, giving the data in the Table 7.23. As with other energies, data presented are with source modulation removed.

Source (Energy)	Q (%)	Q-error (%)	U (%)	U-error (%)	Mod (%)	Mod-error (%)	Phi (rad)	Phi-error (rad)
Al K (1.5 keV)	-0.47	0.11	-0.18	0.11	0.5	0.11	-1.39	0.11

**Table 7.23:** Spurious modulation measurement at 1.5 keV after source modulation removal.

Figure 7.1 compares the spurious modulation measured at 3 energies during telescope calibration at MSFC (orange) with measurements of the detector (DU1) at IAPS (blue). Although the energies are not all the same, it is evident that the two data sets are in good agreement. This demonstrates that the presence of the MMA has no effect on spurious modulation, such that values measured during detector calibration remain valid for telescope performance.

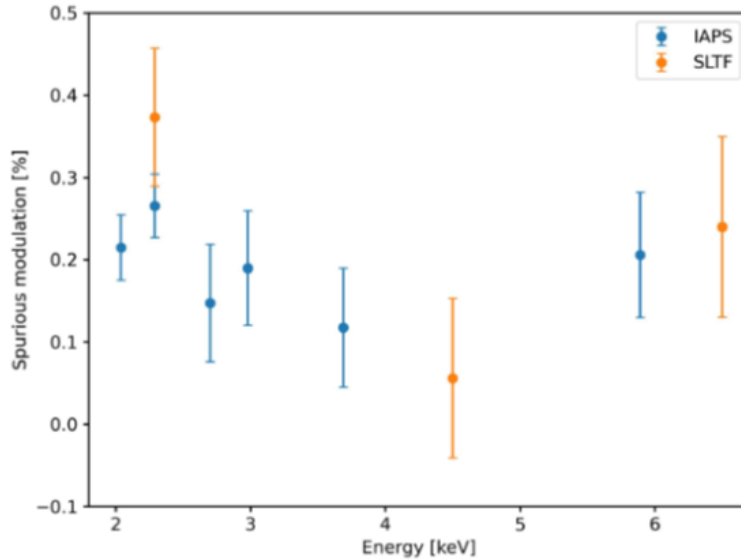


**Figure 7.1:** Spurious modulation data taken for the telescope at the SLTF and for the DU alone in Italy

An additional set of measurements were performed at SLTF at 2.3 keV, where the spurious modulation was measured for the telescope and then for the DU alone, after moving from behind the optic so that it was directly illuminated by the source. For the latter measurement, an electronic mask was applied to the DU so that only events within the dither radius were registered (as for the modulation factor measurements).

As Table 7.24 shows, the spurious modulation measured with the telescope (top row) is statistically identical to that measured for the DU alone (bottom row). As with the modulation factor, the spurious modulation is unchanged by the presence of the optic.

Source (Energy)	Q (%)	Q-error (%)	U (%)	U-error (%)	Mod (%)	Mod-error (%)	Phi (rad)	Phi-error (rad)	MMA
Mo L (2.3 keV)	-0.489	0.089	0.207	0.089	0.531	0.089	1.370	0.084	Yes
Mo L (2.3 keV)	-0.40	0.10	0.08	0.10	0.41	0.10	1.48	0.12	No

**Table 7.24:** Spurious modulation measurement results at 2.3 keV with and without the MMA

The above data show that the MMA has no effect on spurious modulation. Figure 7.1 compares data taken during telescope calibration with data taken with the same DU during detector calibration in Italy. These spurious modulation data are in good agreement. Table 7.24 shows measurements at 2.3 keV both at the focus of MMA4 and then in the direct beam at the SLTF without the optic. The spurious modulation (Mod %) for the two measurements are within 1- $\sigma$  of each other (see Mod-error column) and so are statistically identical.

IXPE Science Operations Center		
Title: User Guide — Observatory	Document No.: IXPE-SOC-DOC-011	Revision: A
	Effective Date: 2022-07-22	Page: 56 of 69

## 8 APPENDIX A: EFFECTIVE-AREA CORRECTION FOR FINITE SOURCE DISTANCE

Analysis of the effective-area correction for finite source distance includes all geometric effects associated with shells and shields. The correction was verified through ray-trace simulations and spot checked with x-ray measurements taken with the beam normal to individual sectors of MMA3 entrance aperture. Data taken in ground calibration have been multiplied by the factor in the table below to give the effective area for infinite source distance.

keV	0 AM	1 AM	2 AM	3 AM	4 AM	5 AM	6 AM	7 AM	8 AM
1.0	1.22	1.20	1.16	1.12	1.09	1.07	1.06	1.05	1.04
1.1	1.22	1.20	1.16	1.12	1.09	1.07	1.06	1.05	1.04
1.2	1.22	1.20	1.16	1.12	1.09	1.07	1.06	1.05	1.04
1.3	1.22	1.20	1.16	1.12	1.09	1.07	1.06	1.05	1.04
1.4	1.22	1.20	1.16	1.12	1.09	1.07	1.06	1.05	1.04
1.5	1.22	1.21	1.17	1.12	1.09	1.07	1.06	1.05	1.04
1.6	1.22	1.21	1.17	1.12	1.09	1.07	1.06	1.05	1.04
1.7	1.22	1.21	1.17	1.12	1.09	1.07	1.06	1.05	1.04
1.8	1.22	1.21	1.17	1.12	1.09	1.07	1.06	1.05	1.04
1.9	1.22	1.21	1.17	1.12	1.09	1.07	1.06	1.05	1.04
2.0	1.22	1.21	1.17	1.12	1.09	1.07	1.06	1.05	1.04
2.1	1.22	1.21	1.17	1.12	1.09	1.07	1.06	1.05	1.04
2.2	1.22	1.21	1.17	1.12	1.09	1.07	1.06	1.05	1.04
2.3	1.22	1.21	1.17	1.12	1.09	1.07	1.06	1.05	1.04
2.4	1.22	1.21	1.17	1.12	1.09	1.07	1.06	1.05	1.04
2.5	1.22	1.21	1.17	1.12	1.09	1.07	1.06	1.05	1.04
2.6	1.22	1.21	1.17	1.12	1.09	1.07	1.06	1.05	1.04
2.7	1.22	1.21	1.17	1.12	1.09	1.07	1.06	1.05	1.04
2.8	1.22	1.21	1.17	1.12	1.09	1.07	1.06	1.05	1.04
2.9	1.22	1.21	1.17	1.12	1.09	1.07	1.06	1.05	1.04
3.0	1.22	1.21	1.17	1.12	1.09	1.07	1.06	1.05	1.04
3.1	1.22	1.21	1.17	1.12	1.09	1.07	1.06	1.05	1.04
3.2	1.22	1.21	1.17	1.12	1.09	1.07	1.06	1.05	1.04
3.3	1.22	1.21	1.17	1.12	1.09	1.07	1.06	1.05	1.04
3.4	1.22	1.21	1.17	1.12	1.09	1.07	1.06	1.05	1.04
3.5	1.22	1.21	1.17	1.12	1.09	1.07	1.06	1.05	1.04
3.6	1.22	1.21	1.17	1.12	1.09	1.07	1.06	1.05	1.04
3.7	1.22	1.21	1.17	1.12	1.09	1.07	1.06	1.05	1.04
3.8	1.22	1.21	1.17	1.12	1.09	1.07	1.06	1.05	1.04
3.9	1.22	1.21	1.17	1.12	1.09	1.07	1.06	1.05	1.04
4.0	1.22	1.21	1.17	1.12	1.09	1.07	1.06	1.05	1.04
4.1	1.22	1.21	1.17	1.12	1.09	1.07	1.06	1.05	1.04

IXPE Science Operations Center									
Title: User Guide — Observatory	Document No.: IXPE-SOC-DOC-011						Revision: A		
	Effective Date: 2022-07-22						Page: 57 of 69		

4.2	1.22	1.21	1.17	1.12	1.09	1.07	1.06	1.05	1.04
4.3	1.22	1.21	1.17	1.12	1.09	1.07	1.06	1.05	1.04
4.4	1.22	1.21	1.17	1.12	1.09	1.07	1.06	1.05	1.04
4.5	1.22	1.21	1.17	1.13	1.09	1.07	1.06	1.05	1.04
4.6	1.22	1.21	1.17	1.13	1.09	1.07	1.06	1.05	1.04
4.7	1.22	1.21	1.17	1.13	1.09	1.07	1.06	1.05	1.04
4.8	1.22	1.21	1.17	1.13	1.09	1.07	1.06	1.05	1.04
4.9	1.23	1.21	1.17	1.13	1.09	1.07	1.06	1.05	1.04
5.0	1.23	1.21	1.17	1.13	1.09	1.07	1.06	1.06	1.05
5.1	1.23	1.21	1.17	1.13	1.09	1.07	1.07	1.06	1.05
5.2	1.23	1.21	1.17	1.13	1.10	1.08	1.07	1.06	1.05
5.3	1.23	1.22	1.18	1.13	1.10	1.08	1.08	1.07	1.06
5.4	1.23	1.22	1.18	1.14	1.10	1.09	1.08	1.07	1.06
5.5	1.23	1.22	1.18	1.14	1.11	1.10	1.09	1.08	1.06
5.6	1.24	1.22	1.19	1.15	1.12	1.10	1.09	1.08	1.05
5.7	1.24	1.23	1.20	1.16	1.13	1.11	1.10	1.08	1.05
5.8	1.25	1.24	1.21	1.17	1.14	1.12	1.10	1.07	1.04
5.9	1.27	1.26	1.23	1.19	1.15	1.13	1.10	1.06	1.03
6.0	1.30	1.29	1.25	1.21	1.16	1.13	1.09	1.05	1.01
6.1	1.34	1.32	1.28	1.22	1.17	1.13	1.08	1.04	1.00
6.2	1.38	1.36	1.30	1.24	1.18	1.12	1.08	1.03	1.00
6.3	1.43	1.40	1.33	1.25	1.18	1.11	1.07	1.02	0.99
6.4	1.47	1.44	1.36	1.27	1.18	1.11	1.06	1.01	0.98
6.5	1.51	1.48	1.39	1.28	1.17	1.10	1.05	1.01	0.98
6.6	1.55	1.52	1.41	1.28	1.17	1.09	1.04	1.00	0.97
6.7	1.59	1.54	1.43	1.29	1.17	1.08	1.03	1.00	0.97
6.8	1.61	1.56	1.43	1.29	1.17	1.08	1.03	0.99	0.97
6.9	1.62	1.57	1.44	1.29	1.16	1.08	1.03	0.99	0.96
7.0	1.63	1.58	1.44	1.29	1.16	1.07	1.02	0.99	0.96
7.1	1.64	1.58	1.44	1.29	1.16	1.07	1.02	0.98	0.96
7.2	1.64	1.58	1.44	1.28	1.15	1.07	1.02	0.98	0.95
7.3	1.64	1.58	1.44	1.28	1.15	1.07	1.01	0.98	0.95
7.4	1.64	1.59	1.44	1.28	1.15	1.06	1.01	0.97	0.95
7.5	1.64	1.59	1.44	1.28	1.15	1.06	1.01	0.97	0.94
7.6	1.65	1.60	1.45	1.28	1.14	1.06	1.00	0.96	0.94
7.7	1.67	1.61	1.45	1.28	1.14	1.05	0.99	0.95	0.93
7.8	1.65	1.59	1.44	1.27	1.14	1.05	0.99	0.95	0.93
7.9	1.66	1.60	1.45	1.27	1.14	1.05	0.99	0.95	0.93
8.0	1.68	1.62	1.46	1.27	1.13	1.04	0.98	0.94	0.93
8.1	1.72	1.65	1.47	1.27	1.12	1.03	0.97	0.94	0.93
8.2	1.76	1.69	1.49	1.28	1.11	1.01	0.95	0.93	0.93

IXPE Science Operations Center		
Title: User Guide — Observatory	Document No.: IXPE-SOC-DOC-011	Revision: A
	Effective Date: 2022-07-22	Page: 58 of 69

8.3	1.81	1.72	1.50	1.26	1.09	0.99	0.95	0.93	0.94
8.4	1.64	1.58	1.40	1.22	1.09	1.01	0.98	0.96	0.96
8.5	1.61	1.55	1.40	1.24	1.11	1.03	0.98	0.96	0.95
8.6	1.62	1.56	1.41	1.24	1.11	1.02	0.98	0.96	0.95
8.7	1.63	1.58	1.42	1.24	1.11	1.02	0.97	0.96	0.95
8.8	1.65	1.59	1.42	1.24	1.10	1.01	0.97	0.95	0.95
8.9	1.67	1.61	1.43	1.24	1.10	1.01	0.97	0.95	0.95
9.0	1.69	1.63	1.44	1.24	1.09	1.01	0.97	0.95	0.95
9.1	1.72	1.65	1.45	1.24	1.09	1.00	0.96	0.95	0.95
9.2	1.74	1.67	1.45	1.24	1.08	0.99	0.96	0.95	0.95
9.3	1.77	1.69	1.46	1.23	1.07	0.99	0.96	0.95	0.95
9.4	1.81	1.71	1.47	1.23	1.07	0.98	0.96	0.95	0.95
9.5	1.84	1.74	1.47	1.22	1.06	0.98	0.96	0.95	0.95
9.6	1.87	1.76	1.48	1.22	1.05	0.98	0.95	0.95	0.95
9.7	1.91	1.79	1.48	1.21	1.05	0.97	0.95	0.95	0.96
9.8	1.95	1.81	1.49	1.20	1.04	0.97	0.95	0.95	0.96
9.9	1.99	1.84	1.49	1.20	1.03	0.97	0.96	0.96	0.96
10.0	2.03	1.86	1.49	1.19	1.03	0.97	0.96	0.96	0.96

**Table A.1:** Ratio of MMA effective areas for infinite and finite source distances as a function of energy and off-axis angle (in arcmin [AM])

IXPE Science Operations Center		
Title: User Guide — Observatory	Document No.: IXPE-SOC-DOC-011	Revision: A
	Effective Date: 2022-07-22	Page: 59 of 69

## 9 APPENDIX B: MMA EFFECTIVE AREAS, CORRECTED TO INIFINITE SOURCE DISTANCE

Energy	MMA1	MMA2	MMA3	Total
keV	cm <sup>2</sup>			
1.02	56.5	55.6	57.6	169.7
1.06	64.2	63.1	65.5	192.9
1.1	71.9	70.7	73.4	216
1.14	78.3	77	79.8	235.1
1.18	84.6	83.2	86.3	254.1
1.22	91	89.4	92.8	273.2
1.26	97.3	95.7	99.3	292.2
1.3	103.6	101.9	105.7	311.3
1.34	108.4	106.6	110.5	325.5
1.38	113.1	111.2	115.4	339.6
1.42	117.8	115.8	120.2	353.8
1.46	122.5	120.5	125	368
1.5	127.2	125.1	129.8	382.2
1.54	128	125.9	130.6	384.5
1.58	128.8	126.6	131.4	386.8
1.62	129.6	127.4	132.2	389.2
1.66	130.4	128.2	133	391.5
1.7	131.1	128.9	133.8	393.9
1.74	134	131.8	136.7	402.5
1.78	136.9	134.6	139.7	411.2
1.82	139.8	137.5	142.6	419.9
1.86	142.7	140.3	145.6	428.5
1.9	145.6	143.1	148.5	437.2
1.94	147.8	145.3	150.7	443.8
1.98	150	147.5	153	450.4
2.02	152.2	149.6	155.2	457
2.06	154.4	151.8	157.5	463.6
2.1	156.6	153.9	159.7	470.2
2.14	158.3	155.6	161.4	475.3
2.18	160	157.3	163.2	480.5
2.22	161.7	159	164.9	485.6
2.26	163.4	160.7	166.7	490.8
2.3	165.1	162.3	168.4	495.9
2.34	166.5	163.7	169.8	499.9
2.38	167.8	165	171.2	504
2.42	169.2	166.3	172.6	508

IXPE Science Operations Center		
<b>Title: User Guide — Observatory</b>	<b>Document No.: IXPE-SOC-DOC-011</b>	<b>Revision: A</b>
	<b>Effective Date: 2022-07-22</b>	<b>Page: 60 of 69</b>

2.46	170.5	167.7	173.9	512.1
2.5	171.9	169	175.3	516.1
2.54	172.9	170	176.4	519.4
2.58	174	171.1	177.5	522.6
2.62	175.1	172.1	178.6	525.8
2.66	176.1	173.2	179.7	529
2.7	177.2	174.2	180.8	532.2
2.74	178.1	175.1	181.6	534.8
2.78	178.9	175.9	182.5	537.3
2.82	179.8	176.7	183.4	539.9
2.86	180.6	177.6	184.2	542.4
2.9	181.4	178.4	185.1	545
2.94	182.1	179.1	185.8	547
2.98	182.8	179.7	186.5	549
3.02	183.5	180.4	187.2	551
3.06	184.1	181.1	187.9	553.1
3.1	184.8	181.7	188.5	555.1
3.14	185.4	182.3	189.1	556.8
3.18	186	182.8	189.7	558.5
3.22	186.5	183.4	190.3	560.2
3.26	187.1	184	190.9	561.9
3.3	187.7	184.5	191.5	563.7
3.34	188.1	185	191.9	565
3.38	188.6	185.4	192.4	566.4
3.42	189	185.9	192.8	567.7
3.46	189.5	186.3	193.3	569.1
3.5	189.9	186.7	193.7	570.4
3.54	190.3	187.1	194.1	571.5
3.58	190.7	187.5	194.5	572.7
3.62	191.1	187.9	194.9	573.8
3.66	191.4	188.2	195.3	575
3.7	191.8	188.6	195.7	576.1
3.74	192.1	188.9	196	577.1
3.78	192.4	189.2	196.3	578
3.82	192.8	189.5	196.6	578.9
3.86	193.1	189.8	197	579.9
3.9	193.4	190.1	197.3	580.8
3.94	193.6	190.4	197.5	581.6
3.98	193.9	190.7	197.8	582.3
4.02	194.2	190.9	198.1	583.1
4.06	194.4	191.2	198.3	583.9
4.1	194.7	191.4	198.6	584.7
4.14	194.9	191.6	198.8	585.3

IXPE Science Operations Center		
<b>Title: User Guide — Observatory</b>	<b>Document No.: IXPE-SOC-DOC-011</b>	<b>Revision: A</b>
	<b>Effective Date: 2022-07-22</b>	<b>Page: 61 of 69</b>

4.18	195.1	191.8	199	585.9
4.22	195.3	192	199.2	586.6
4.26	195.5	192.2	199.4	587.2
4.3	195.7	192.4	199.7	587.8
4.34	195.9	192.6	199.8	588.3
4.38	196	192.7	200	588.7
4.42	196.2	192.9	200.1	589.2
4.46	196.3	193	200.3	589.7
4.5	196.5	193.2	200.4	590.1
4.54	196.6	193.3	200.6	590.6
4.58	196.8	193.5	200.7	591
4.62	196.9	193.6	200.9	591.4
4.66	197	193.7	201	591.8
4.7	197.2	193.9	201.2	592.2
4.74	197.3	194	201.2	592.5
4.78	197.4	194.1	201.3	592.7
4.82	197.4	194.1	201.4	593
4.86	197.5	194.2	201.5	593.3
4.9	197.6	194.3	201.6	593.5
4.94	197.7	194.4	201.6	593.7
4.98	197.7	194.4	201.7	593.8
5.02	197.8	194.5	201.8	594
5.06	197.8	194.5	201.8	594.1
5.1	197.9	194.6	201.9	594.3
5.14	197.9	194.6	201.9	594.3
5.18	197.9	194.6	201.9	594.4
5.22	197.9	194.6	201.9	594.4
5.26	197.9	194.6	201.9	594.5
5.3	198	194.6	201.9	594.6
5.34	197.9	194.6	201.9	594.5
5.38	197.9	194.6	201.9	594.4
5.42	197.9	194.6	201.9	594.4
5.46	197.9	194.6	201.9	594.3
5.5	197.9	194.6	201.9	594.3
5.54	197.8	194.5	201.8	594.1
5.58	197.7	194.4	201.7	593.9
5.62	197.7	194.4	201.6	593.7
5.66	197.6	194.3	201.6	593.5
5.7	197.5	194.2	201.5	593.3
5.74	197.4	194.1	201.4	592.9
5.78	197.3	194	201.3	592.5
5.82	197.2	193.9	201.1	592.2
5.86	197	193.7	201	591.8

IXPE Science Operations Center		
Title: User Guide — Observatory	Document No.: IXPE-SOC-DOC-011	Revision: A
	Effective Date: 2022-07-22	Page: 62 of 69

5.9	196.9	193.6	200.9	591.4
5.94	196.7	193.4	200.7	590.8
5.98	196.5	193.2	200.4	590.1
6.02	196.2	193	200.2	589.4
6.06	196	192.7	200	588.7
6.1	195.8	192.5	199.7	588.1
6.14	195.4	192.1	199.4	586.9
6.18	195	191.8	199	585.8
6.22	194.7	191.4	198.6	584.6
6.26	194.3	191	198.2	583.5
6.3	193.9	190.7	197.8	582.3
6.34	193.1	189.9	197	580
6.38	192.3	189.1	196.2	577.7
6.42	191.6	188.4	195.4	575.3
6.46	190.8	187.6	194.6	573
6.5	190	186.8	193.8	570.7
6.54	188.3	185.2	192.1	565.6
6.58	186.7	183.5	190.4	560.6
6.62	185	181.9	188.7	555.6
6.66	183.3	180.2	187	550.5
6.7	181.6	178.6	185.3	545.5
6.74	179	176	182.6	537.6
6.78	176.4	173.4	180	529.8
6.82	173.8	170.9	177.3	522
6.86	171.2	168.3	174.6	514.1
6.9	168.6	165.7	172	506.3
6.94	165.7	162.9	169	497.6
6.98	162.8	160	166	488.8
7.02	159.9	157.2	163.1	480.1
7.06	157	154.3	160.1	471.4
7.1	154	151.5	157.1	462.7
7.14	151.1	148.6	154.1	453.8
7.18	148.2	145.7	151.1	445
7.22	145.2	142.8	148.2	436.2
7.26	142.3	139.9	145.2	427.3
7.3	139.3	137	142.2	418.5
7.34	136.4	134.1	139.2	409.7
7.38	133.5	131.3	136.2	401
7.42	130.6	128.4	133.2	392.2
7.46	127.7	125.5	130.2	383.4
7.5	124.7	122.7	127.3	374.6
7.54	120.3	118.3	122.7	361.4
7.58	115.9	113.9	118.2	348.1

IXPE Science Operations Center		
Title: User Guide — Observatory	Document No.: IXPE-SOC-DOC-011	Revision: A
	Effective Date: 2022-07-22	Page: 63 of 69

7.62	111.5	109.6	113.7	334.8
7.66	107	105.2	109.2	321.5
7.7	102.6	100.9	104.7	308.2
7.74	99.2	97.5	101.2	298
7.78	95.8	94.2	97.7	287.7
7.82	92.4	90.8	94.3	277.5
7.86	89	87.5	90.8	267.3
7.9	85.6	84.1	87.3	257
7.94	83.4	82	85.1	250.5
7.98	81.2	79.9	82.9	243.9
8.02	79	77.7	80.6	237.4
8.06	76.9	75.6	78.4	230.9
8.1	74.7	73.4	76.2	224.3
8.14	66.7	65.6	68	200.3
8.18	58.7	57.7	59.9	176.3
8.22	50.7	49.9	51.7	152.4
8.26	42.7	42	43.6	128.4
8.3	34.8	34.2	35.5	104.4
8.34	33.4	32.9	34.1	100.4
8.38	32.1	31.6	32.8	96.5
8.42	30.8	30.3	31.4	92.5
8.46	29.5	29	30.1	88.6
8.5	28.2	27.7	28.7	84.6
8.54	28.3	27.8	28.9	85
8.58	28.4	27.9	29	85.4
8.62	28.5	28.1	29.1	85.7
8.66	28.7	28.2	29.2	86.1
8.7	28.8	28.3	29.4	86.5
8.74	28.5	28.1	29.1	85.7
8.78	28.3	27.8	28.9	85
8.82	28.1	27.6	28.6	84.3
8.86	27.8	27.4	28.4	83.5
8.9	27.6	27.1	28.1	82.8
8.94	27.2	26.8	27.8	81.7
8.98	26.8	26.4	27.4	80.6
9.02	26.5	26	27	79.6
9.06	26.1	25.7	26.6	78.5
9.1	25.8	25.3	26.3	77.4
9.14	25.3	24.9	25.9	76.1
9.18	24.9	24.5	25.4	74.9
9.22	24.5	24.1	25	73.6
9.26	24.1	23.7	24.6	72.4
9.3	23.7	23.3	24.2	71.1

IXPE Science Operations Center		
<b>Title: User Guide — Observatory</b>	<b>Document No.: IXPE-SOC-DOC-011</b>	<b>Revision: A</b>
	<b>Effective Date: 2022-07-22</b>	<b>Page: 64 of 69</b>

9.34	23.3	22.9	23.7	69.8
9.38	22.8	22.4	23.3	68.5
9.42	22.4	22	22.8	67.2
9.46	22	21.6	22.4	65.9
9.5	21.5	21.2	22	64.6
9.54	21.1	20.7	21.5	63.3
9.58	20.7	20.3	21.1	62.1
9.62	20.2	19.9	20.6	60.8
9.66	19.8	19.5	20.2	59.5
9.7	19.4	19	19.8	58.2
9.74	18.9	18.6	19.3	56.8
9.78	18.5	18.2	18.8	55.5
9.82	18	17.7	18.4	54.1
9.86	17.6	17.3	17.9	52.8
9.9	17.1	16.8	17.5	51.4
9.94	16.7	16.4	17	50.1
9.98	16.3	16	16.6	48.8
10.02	15.8	15.6	16.1	47.5
10.06	15.4	15.1	15.7	46.2
10.1	15	14.7	15.3	44.9
10.14	14.6	14.3	14.9	43.7
10.18	14.2	13.9	14.4	42.5
10.22	13.8	13.5	14	41.3
10.26	13.4	13.1	13.6	40.1
10.3	13	12.7	13.2	38.9
10.34	12.6	12.4	12.8	37.8
10.38	12.2	12	12.4	36.6
10.42	11.8	11.6	12	35.4
10.46	11.4	11.2	11.6	34.2
10.5	11	10.8	11.2	33
10.54	10.6	10.4	10.8	31.8
10.58	10.2	10	10.4	30.7
10.62	9.8	9.7	10	29.5
10.66	9.5	9.3	9.6	28.4
10.7	9.1	8.9	9.3	27.3
10.74	8.7	8.6	8.9	26.2
10.78	8.4	8.2	8.6	25.2
10.82	8	7.9	8.2	24.1
10.86	7.7	7.6	7.8	23.1
10.9	7.3	7.2	7.5	22.1
10.94	7	6.9	7.2	21.1
10.98	6.7	6.6	6.9	20.2
11.02	6.4	6.3	6.5	19.3

IXPE Science Operations Center		
Title: User Guide — Observatory	Document No.: IXPE-SOC-DOC-011	Revision: A
	Effective Date: 2022-07-22	Page: 65 of 69

11.06	6.1	6	6.2	18.3
11.1	5.8	5.7	5.9	17.4
11.14	5.5	5.4	5.6	16.6
11.18	5.2	5.2	5.3	15.7
11.22	5	4.9	5.1	14.9
11.26	4.7	4.6	4.8	14.1
11.3	4.4	4.3	4.5	13.2
11.34	4.2	4.1	4.3	12.6
11.38	4	3.9	4	11.9
11.42	3.7	3.7	3.8	11.2
11.46	3.5	3.5	3.6	10.5
11.5	3.3	3.2	3.4	9.9
11.54	3.1	3.1	3.2	9.3
11.58	2.9	2.9	3	8.8
11.62	2.8	2.7	2.8	8.3
11.66	2.6	2.5	2.6	7.8
11.7	2.4	2.4	2.5	7.3
11.74	2.3	2.2	2.3	6.9
11.78	2.1	2.1	2.2	6.4
11.82	2	2	2	6
11.86	1.9	1.8	1.9	5.6
11.9	1.7	1.7	1.8	5.2
11.94	1.6	1.6	1.7	4.9
11.98	1.5	1.5	1.6	4.6

**Table B.1:** MMA effective areas corrected to infinite source distance.

IXPE Science Operations Center		
Title: User Guide — Observatory	Document No.: IXPE-SOC-DOC-011	Revision: A
	Effective Date: 2022-07-22	Page: 66 of 69

## 10 APPENDIX C: ACRONYM LIST

ADCS	Attitude Determination and Control System
ASI	Agenzia Spaziale Italiana (Italian Space Agency)
ASIC	Application Specific Integrated Circuit
CCD	Charge Coupled Device
DME	Dimethyl Ether
DU	Detector Unit
DSU	Detectors Service Unit
FCW	Filter and Calibration Wheel
FDIR	Fault Detection Isolation and Recovery
FITS	Flexible Image Transport System
FWHM	Full Width at Half Maximum Height
GEM	Gas Electron Multiplier
GPD	Gas Pixel Detector
GPS	Global Positioning System
HEASARC	High Energy Astrophysics Science Archive Research Center
HPD	Half Power Diameter
HV	High Voltage
IAPS	Istituto di Astrofisica e Planetologia Spaziali
IAU	Integrated Avionics Unit
INAF	Istituto Nazionale di Astrofisica
INFN	Istituto Nazionale di Fisica Nucleare
IXPE	Imaging X-ray Polarimetry Explorer
I2T	Italian Instrument Team
LASP	Laboratory for Atmospheric and Space Research
MMA	Mirror Module Assembly
MOC	Mission Operation Center

IXPE Science Operations Center		
Title: User Guide — Observatory	Document No.: IXPE-SOC-DOC-011	Revision: A
	Effective Date: 2022-07-22	Page: 67 of 69

MRAM	Magnetoresistive Random Access Memory
MSFC	Marshall Space Flight Center
MMSS	Mirror Module Support Structure
NASA	National Aeronautics and Space Administration
OBT	On-Board Timing
PI	Principal Investigator
PPS	Pulse Per Second
PROM	Programmable Read Only Memory
PSF	Point Spread Function
ROI	Region of Interest
SAA	South Atlantic Anomaly
SDD	Silicon Drift Detector
SLTF	Stray Light Test Facility
SMR	Surface Mount Reflector
SOC	Science Operation Center
SRAM	Static Random Access Memory
SSDC	Space Science Data Center
TM	Telemetry
TOD	Time of Day
TTR	Tip Tilt Rotate
TXCO	Temperature Compensated Crystall Oscillator
UV	Ultraviolet

IXPE Science Operations Center		
Title: User Guide — Observatory	Document No.: IXPE-SOC-DOC-011	Revision: A
	Effective Date: 2022-07-22	Page: 68 of 69

## 11 REFERENCES

- <sup>1</sup> Ramsey, B.D., Bongiorno, S.B., Kolodziejczak, J.K., Kilaru, K., Alexander, C., Baumgartner, W.H., Elsner, R.F., McCracken, J., Mitsuishi, I., Pavelitz, S.D., Ranganathan, J., Sanchez, J., Speegle, C.O., Weddendorf, B., and O'Dell, S.L., "IXPE Mirror Module Assemblies," SPIE 11119, 1111903 (2019).
- <sup>2</sup> Costa, E., Soffitta, P., Bellazzini, R., Brez, A., Lumb, N., and Spandre, G., "An efficient photoelectric X-ray polarimeter for the study of black holes and neutron stars," *Nature* 411, 662-665 (2001).
- <sup>3</sup> Bellazzini, R., Spandre, G., Minuti, M., Baldini, L., Brez, A., Latronico, L., Omodei, N., Razzano, M., Massai, M., Pesce-Rollins, M., Sgro, C., Costa, E., Soffitta, P., Sipila, H., and Lempinen, E., "A sealed Gas Pixel Detector for X-ray astronomy," *NIMPA* 579, 853-858 (2007).
- <sup>4</sup> Baldini, L., Barbanera, M., Bellazzini, R., Bonino, R., Borotto, F., Brez, A., Caporale, C., Cardelli, C., Castellano, S., Ceccanti, M., Citraro, S., Di Lalla, N., Latronico, L., Lucchesi, L., Magazzù, C., Magazzù, G., Maldera, S., Manfreda, A., Marengo, M., Marrocchesi, A., Mereu, P., Minuti, M., Mosti, F., Nasimi, H., Nuti, A., Oppedisano, C., Orsini, L., Pesce-Rollins, M., Pinchera, M., Profeti, A., Sgrò, C., Spandre, G., Tardiola, M., Zanetti, D., Amici, F., Andersson, H., Attinà, P., Bachetti, M., Baumgartner, W., Brienza, D., Carpentiero, R., Castronuovo, M., Cavalli, L., Cavazzuti, E., Centrone, M., Costa, E., D'Alba, E., D'Amico, F., Del Monte, E., Di Cosimo, S., Di Marco, A., Di Persio, G., Donnarumma, I., Evangelista, Y., Fabiani, S., Ferrazzoli, R., Kitaguchi, T., La Monaca, F., Lefevre, C., Loffredo, P., Lorenzi, P., Mangraviti, E., Matt, G., Meilähti, T., Morbidini, A., Muleri, F., Nakano, T., Negri, B., Nenonen, S., O'Dell, S.L., Perri, M., Piazzolla, R., Pieraccini, S., Pilia, M., Puccetti, S., Ramsey, B.D., Rankin, J., Ratheesh, A., Rubini, A., Santoli, F., Sarra, P., Scalise, E., Sciortino, A., Soffitta, P., Tamagawa, T., Tennant, A.F., Tobia, A., Trois, A., Uchiyama, K., Vimercati, M., Weisskopf, M.C., Xie, F., Zanetti, F., and Zhou, Y., "Design, construction, and test of the Gas Pixel Detectors for the IXPE mission," *Aph* 133, 102628 (2021).
- <sup>5</sup> Rankin, J., Muleri, F., Tennant, A.F., Bachetti, M., Costa, E., Marco, A.D., Fabiani, S., La Monaca, F., Soffitta, P., Tobia, A., Trois, A., Xie, F., Baldini, L., Di Lalla, N., Manfreda, A., O'Dell, S.L., Perri, M., Puccetti, S., Ramsey, B.D., Sgrò, C., and Weisskopf, M.C., "An Algorithm to Calibrate and Correct the Response to Unpolarized Radiation of the X-Ray Polarimeter Onboard IXPE," *AJ* 163, 39 (2022).
- <sup>6</sup> Di Marco, A., Costa, E., Muleri, F., Soffitta, P., Fabiani, S., La Monaca, F., Rankin, J., Xie, F., Bachetti, M., Baldini, L., Baumgartner, W., Bellazzini, R., Brez, A., Castellano, S., Del Monte, E., Di Lalla, N., Ferrazzoli, R., Latronico, L., Maldera, S., Manfreda, A., O'Dell, S.L., Perri, M., Pesce-Rollins, M., Puccetti, S., Ramsey, B.D., Ratheesh, A., Sgrò, C., Spandre, G., Tennant, A.F., Tobia, A., Trois, A., and Weisskopf, M.C., "A Weighted Analysis to Improve the X-Ray Polarization Sensitivity of the Imaging X-ray Polarimetry Explorer," *AJ* 163, 170 (2022).
- <sup>7</sup> Muleri F. et al., 'Response of the IXPE Detector Units to unpolarized radiation' in preparation (2021). @@@
- <sup>8</sup> Rankin, J., Muleri, F., Tennant, A.F., Bachetti, M., Costa, E., Marco, A.D., Fabiani, S., La Monaca, F., Soffitta, P., Tobia, A., Trois, A., Xie, F., Baldini, L., Di Lalla, N., Manfreda, A., O'Dell, S.L., Perri, M., Puccetti, S., Ramsey, B.D., Sgrò, C., and Weisskopf, M.C., "An Algorithm to Calibrate and Correct the Response to Unpolarized Radiation of the X-Ray Polarimeter Onboard IXPE," *AJ* 163, 39 (2022).
- <sup>9</sup> Xie, F., Ferrazzoli, R., Soffitta, P., Fabiani, S., Costa, E., Muleri, F., and Marco, D., "A study of background for IXPE," *Aph* 128, 102566 (2021).
- <sup>10</sup> Ferrazzoli, R., Muleri, F., Lefevre, C., Morbidini, A., Amici, F., Brienza, D., Costa, E., Del Monte, E., Di Marco, A., Di Persio, G., Donnarumma, I., Fabiani, S., La Monaca, F., Loffredo, P., Maiolo, L., Maita, F., Piazzolla, R., Ramsey, B., Rankin, J., Ratheesh, A., Rubini, A., Sarra, P., Soffitta, P., Tobia, A., and Xie, F., "In-flight calibration system of imaging x-ray polarimetry explorer," *JATIS* 6, 048002 (2020).
- <sup>11</sup> Li, T., Zeng, M., Feng, H., Cang, J., Li, H., Zhang, H., Zeng, Z., Cheng, J., Ma, H., and Liu, Y., "Electron track reconstruction and improved modulation for photoelectric X-ray polarimetry," *NIMPA* 858, 62-68 (2017).
- <sup>12</sup> Kitaguchi, T., Black, K., Enoto, T., Fukazawa, Y., Hayato, A., Hill, J.E., Iwakiri, W.B., Jahoda, K., Kaaret, P., McCurdy, R., Mizuno, T., Nakano, T., and Tamagawa, T., "An optimized photoelectron track reconstruction method for photoelectric x-ray polarimeters," *NIMPA* 880, 188-193 (2018).

IXPE Science Operations Center		
Title: User Guide — Observatory	Document No.: IXPE-SOC-DOC-011	Revision: A
	Effective Date: 2022-07-22	Page: 69 of 69

<sup>13</sup> Kitaguchi, T., Black, K., Enoto, T., Hayato, A., Hill, J.E., Iwakiri, W.B., Kaaret, P., Mizuno, T., and Tamagawa, T., “A convolutional neural network approach for reconstructing polarization information of photoelectric X-ray polarimeters,” NIMPA 942, 162389 (2019).

<sup>14</sup> Bellazzini, R., Angelini, F., Baldini, L., Brez, A., Costa, E., Di Persio, G., Latronico, L., Massai, M.M., Omodei, N., Pacciani, L., Soffitta, P., and Spandre, G., “Novel gaseous X-ray polarimeter: data analysis and simulation,” SPIE 4843, 383-393 (2003)

<sup>15</sup> Peirson, A.L., Romani, R.W., Marshall, H.L., Steiner, J.F., and Baldini, L., “Deep ensemble analysis for Imaging X-ray Polarimetry,” NIMPA 986, 164740 (2021).

<sup>16</sup> Peirson, A.L. and Romani, R.W., “Toward Optimal Signal Extraction for Imaging X-Ray Polarimetry,” ApJ 920, 40 (2021).

<sup>17</sup> Xu, X., Ester, M., Kriegel, H.-P., and Sander, J., “Clustering and knowledge discovery in spatial databases,” VA 41, 397-403 (1997).

<sup>18</sup> Baldini, L., Barbanera, M., Bellazzini, R., Bonino, R., Borotto, F., Brez, A., Caporale, C., Cardelli, C., Castellano, S., Ceccanti, M., Citraro, S., Di Lalla, N., Latronico, L., Lucchesi, L., Magazzù, C., Magazzù, G., Maldera, S., Manfreda, A., Marengo, M., Marrocchesi, A., Mereu, P., Minuti, M., Mosti, F., Nasimi, H., Nuti, A., Oppedisano, C., Orsini, L., Pesce-Rollins, M., Pinchera, M., Profeti, A., Sgrò, C., Spandre, G., Tardiola, M., Zanetti, D., Amici, F., Andersson, H., Attinà, P., Bachetti, M., Baumgartner, W., Brienza, D., Carpentiero, R., Castronuovo, M., Cavalli, L., Cavazzuti, E., Centrone, M., Costa, E., D'Alba, E., D'Amico, F., Del Monte, E., Di Cosimo, S., Di Marco, A., Di Persio, G., Donnarumma, I., Evangelista, Y., Fabiani, S., Ferrazzoli, R., Kitaguchi, T., La Monaca, F., Lefevre, C., Loffredo, P., Lorenzi, P., Mangraviti, E., Matt, G., Meilahti, T., Morbidini, A., Muleri, F., Nakano, T., Negri, B., Nenonen, S., O'Dell, S.L., Perri, M., Piazzolla, R., Pieraccini, S., Pilia, M., Puccetti, S., Ramsey, B.D., Rankin, J., Ratheesh, A., Rubini, A., Santoli, F., Sarra, P., Scalise, E., Sciortino, A., Soffitta, P., Tamagawa, T., Tennant, A.F., Tobia, A., Trois, A., Uchiyama, K., Vimercati, M., Weisskopf, M.C., Xie, F., Zanetti, F., and Zhou, Y., “Design, construction, and test of the Gas Pixel Detectors for the IXPE mission,” APh 133, 102628 (2021).

<sup>19</sup> Soffitta, P., Baldini, L., Bellazzini, R., Costa, E., Latronico, L., Muleri, F., Del Monte, E., Fabiani, S., Minuti, M., Pinchera, M., Sgrò, C., Spandre, G., Trois, A., Amici, F., Andersson, H., Attina', P., Bachetti, M., Barbanera, M., Borotto, F., Brez, A., Brienza, D., Caporale, C., Cardelli, C., Carpentiero, R., Castellano, S., Castronuovo, M., Cavalli, L., Cavazzuti, E., Ceccanti, M., Centrone, M., Ciprini, S., Citraro, S., D'Amico, F., D'Alba, E., Di Cosimo, S., Di Lalla, N., Di Marco, A., Di Persio, G., Donnarumma, I., Evangelista, Y., Ferrazzoli, R., Hayato, A., Kitaguchi, T., La Monaca, F., Lefevre, C., Loffredo, P., Lorenzi, P., Lucchesi, L., Magazzu, C., Maldera, S., Manfreda, A., Mangraviti, E., Marengo, M., Matt, G., Mereu, P., Morbidini, A., Mosti, F., Nakano, T., Nasimi, H., Negri, B., Nenonen, S., Nuti, A., Orsini, L., Perri, M., Pesce-Rollins, M., Piazzolla, R., Pilia, M., Profeti, A., Puccetti, S., Rankin, J., Ratheesh, A., Rubini, A., Santoli, F., Sarra, P., Scalise, E., Sciortino, A., Tamagawa, T., Tardiola, M., Tobia, A., Vimercati, M., and Xie, F., “The Instrument of the Imaging X-Ray Polarimetry Explorer,” AJ 162, 208 (2021).

<sup>20</sup> Rankin, J., Muleri, F., Tennant, A.F., Bachetti, M., Costa, E., Marco, A.D., Fabiani, S., La Monaca, F., Soffitta, P., Tobia, A., Trois, A., Xie, F., Baldini, L., Di Lalla, N., Manfreda, A., O'Dell, S.L., Perri, M., Puccetti, S., Ramsey, B.D., Sgrò, C., and Weisskopf, M.C., “An Algorithm to Calibrate and Correct the Response to Unpolarized Radiation of the X-Ray Polarimeter Onboard IXPE,” AJ 163, 39 (2022).

<sup>21</sup> Muleri, F., Piazzolla, R., Di Marco, A., Fabiani, S., La Monaca, F., Lefevre, C., Morbidini, A., Rankin, J., Soffitta, P., Tobia, A., Xie, F., Amici, F., Attinà, P., Bachetti, M., Brienza, D., Centrone, M., Costa, E., Del Monte, E., Di Cosimo, S., Di Persio, G., Evangelista, Y., Ferrazzoli, R., Loffredo, P., Perri, M., Pilia, M., Puccetti, S., Ratheesh, A., Rubini, A., Santoli, F., Scalise, E., and Trois, A., “The IXPE instrument calibration equipment,” APh 136, 102658 (2022).

<sup>22</sup> Di Marco, A., Costa, E., Muleri, F., Soffitta, P., Fabiani, S., La Monaca, F., Rankin, J., Xie, F., Bachetti, M., Baldini, L., Baumgartner, W., Bellazzini, R., Brez, A., Castellano, S., Del Monte, E., Di Lalla, N., Ferrazzoli, R., Latronico, L., Maldera, S., Manfreda, A., O'Dell, S.L., Perri, M., Pesce-Rollins, M., Puccetti, S., Ramsey, B.D., Ratheesh, A., Sgrò, C., Spandre, G., Tennant, A.F., Tobia, A., Trois, A., and Weisskopf, M.C., “A Weighted Analysis to Improve the X-Ray Polarization Sensitivity of the Imaging X-ray Polarimetry Explorer,” AJ 163, 170 (2022).